

AD-A053 467

CALIFORNIA RESEARCH AND TECHNOLOGY INC WOODLAND HILLS
SENSITIVITY STUDY OF THE HUSKY PUP GRANITE BLOCK EXPERIMENT. (U)

F/G 19/4

MAR 77 S H SCHUSTER, K N KREYENHAGEN

DNA001-76-C-0345

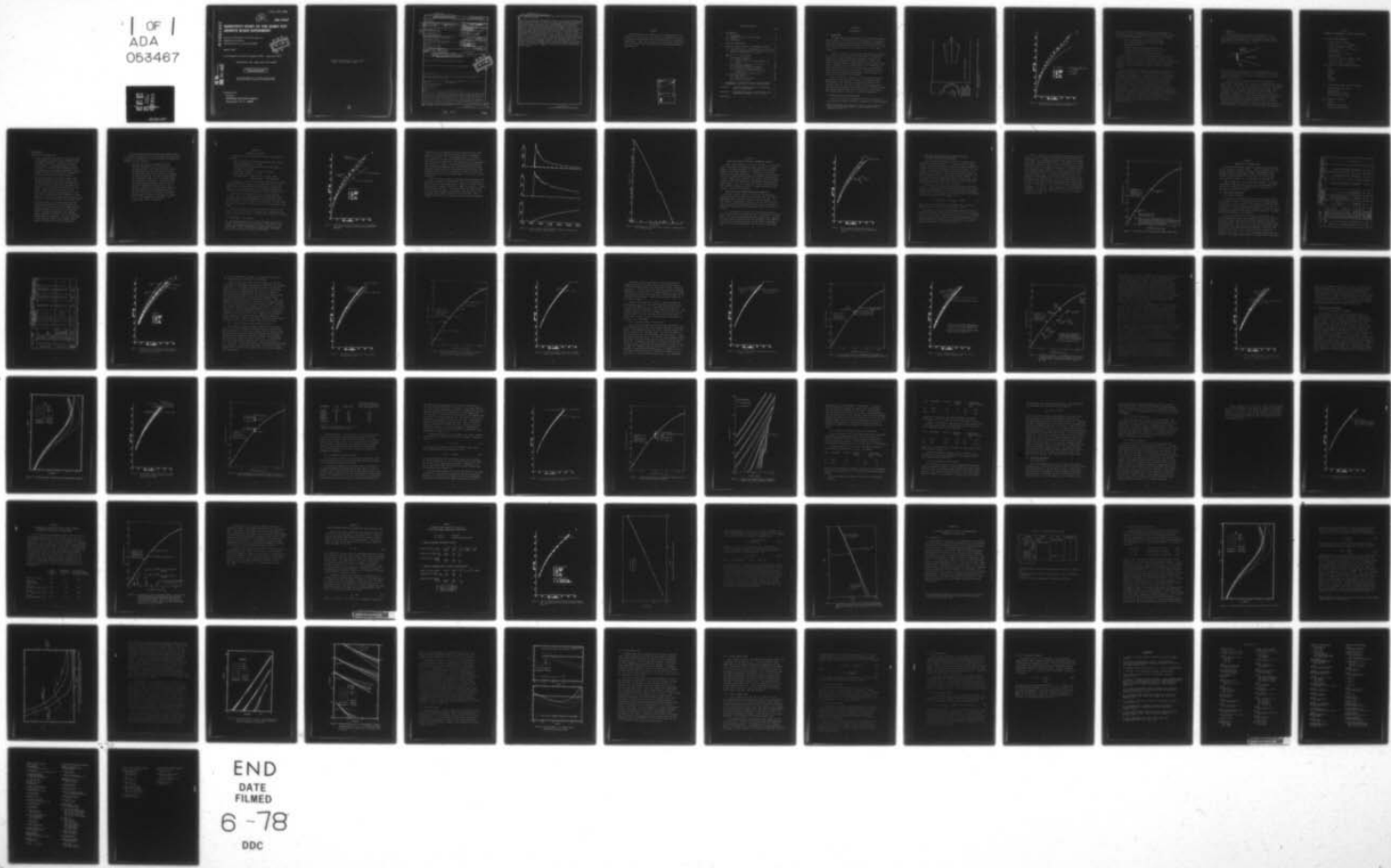
UNCLASSIFIED

CRT-3110-1

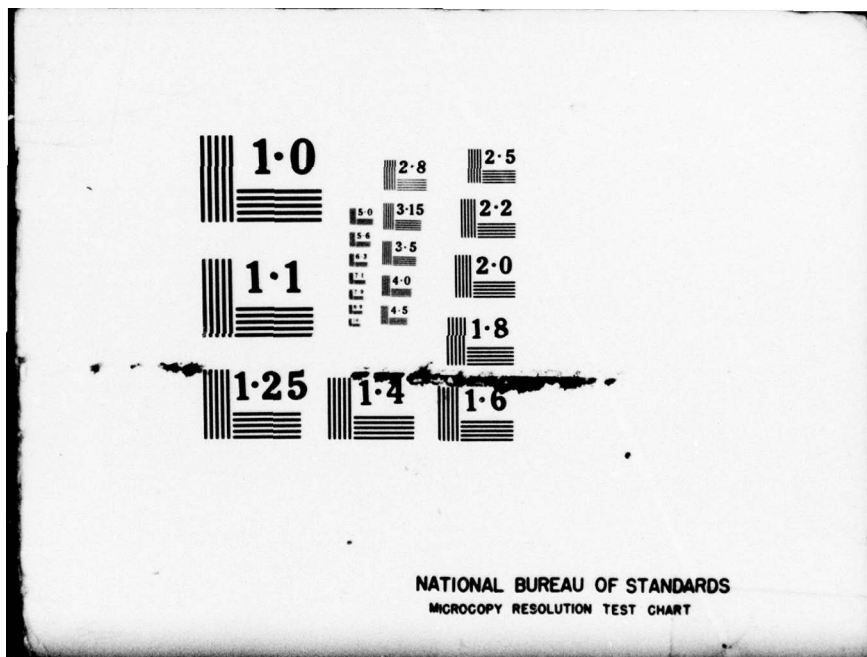
DNA-4263F

NL

1 OF
ADA
063467



END
DATE
FILED
6 - 78
DDC



AD A 053467

AD-E300 186

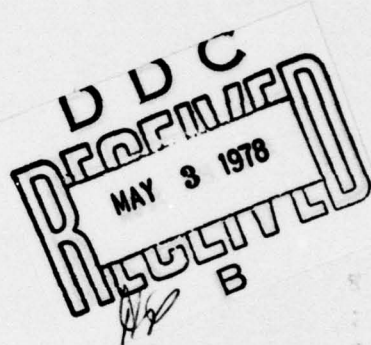
(12) *5A*

DNA 4263F

SENSITIVITY STUDY OF THE HUSKY PUP GRANITE BLOCK EXPERIMENT

California Research & Technology, Inc.
6269 Variel Avenue
Woodland Hills, California 91367

March 1977



Final Report for Period August 1976 – February 1977

CONTRACT No. DNA 001-76-C-0345

APPROVED FOR PUBLIC RELEASE;
DISTRIBUTION UNLIMITED.

AD No.
DDC FILE COPY
DDC

THIS WORK SPONSORED BY THE DEFENSE NUCLEAR AGENCY
UNDER RDT&E RMSS CODE B34407T462 L41AAXSX34003 H2590D.

Prepared for

Director

DEFENSE NUCLEAR AGENCY

Washington, D. C. 20305

Destroy this report when it is no longer
needed. Do not return to sender.



UNCLASSIFIED

SECURITY CLASSIFICATION OF THIS PAGE (When Data Entered)

REPORT DOCUMENTATION PAGE		READ INSTRUCTIONS BEFORE COMPLETING FORM
1. REPORT NUMBER DNA 4263F	2. GOVT ACCESSION NO.	3. RECIPIENT'S CATALOG NUMBER
4. TITLE (and Subtitle) SENSITIVITY STUDY OF THE HUSKY PUP GRANITE BLOCK EXPERIMENT.		5. TYPE OF REPORT & PERIOD COVERED Final Report, for Period Aug 76—Feb 77
6. AUTHOR S. H. Schuster K. N. Kreyenhagen		7. PERFORMING ORG. REPORT NUMBER CRT-3110-1
8. CONTRACT OR GRANT NUMBER(s) DNA 001-76-C-0345		9. PERFORMANCE ORGANIZATION NAME AND ADDRESS California Research & Technology, Inc. 6269 Variel Avenue Woodland Hills, California 91367
10. CONTROLLING OFFICE NAME AND ADDRESS Director Defense Nuclear Agency Washington, D.C. 20305		11. PROGRAM ELEMENT, PROJECT, TASK AREA & WORK UNIT NUMBERS NWED Subtask 17 X 340 L41AAXSX340-03
12. REPORT DATE March 1977		13. NUMBER OF PAGES 84
14. MONITORING AGENCY NAME & ADDRESS (if different from Controlling Office) DNA, SBE		15. SECURITY CLASS (of this report) UNCLASSIFIED
16. DISTRIBUTION STATEMENT Approved for public release; distribution unlimited.		17. DISTRIBUTION STATEMENT (of the abstract entered in Block 20, if different from Report) 627104
18. SUPPLEMENTARY NOTES This work sponsored by the Defense Nuclear Agency under RDT&E RMSS Code B34407T462 L41AAXSX34003 H2590D.		
19. KEY WORDS (Continue on reverse side if necessary and identify by block number) HUSKY PUP High Pressure Granite Equation-of-State Numerical Sensitivity Time-of-Arrival Impact		
20. ABSTRACT (Continue on reverse side if necessary and identify by block number) A series of 1-D calculations simulating the impact of the flyer plate on the granite block in the HUSKY PUP experiment was made to evaluate the effects of equation of state (EOS) modeling, energy levels and distributions, and numerical parameters on the resulting time of arrival (TOA) of the shock wave at stations in the block. This objective was to provide a basis for judging the significance of comparisons between TOA vs depth measurements and results of more complex 2-D pretest calculations of the event. The total energy in the		

DD FORM 1 JAN 73 EDITION OF 1 NOV 65 IS OBSOLETE

UNCLASSIFIED
SECURITY CLASSIFICATION OF THIS PAGE (When Data Entered)

next page

391 223

JOB

UNCLASSIFIED

SECURITY CLASSIFICATION OF THIS PAGE(When Data Entered)

20. ABSTRACT (Continued)

flyer plate and block prior to impact was found to be the single most important factor affecting the TOA. Distribution of energy was of secondary importance; internal energy was found to have an effect equivalent to that from about 3/4 of the same quantity of kinetic energy. Eight EOS models for granite were considered. Despite considerable differences in the Hugoniots and release adiabats in these models, the maximum effect of the models on the TOA vs depth curves was equivalent to only a 30 percent change in the flyer plate energy (which presumably directly reflects the source energy). Variations in other parameters, including computational zone size, artificial viscosity, and flyer plate density, had negligible effects on the TOA over the ranges considered. These 1-D results indicate that TOA vs depth calculations are relatively insensitive to any parameter or uncertainty other than the total energy in the flyer plate-granite block system. The reasonably close agreement which has been obtained between measured times of arrival and values calculated in two of the pretest 2-D analyses of the granite block experiment therefore indicates that current code technology is adequate to calculate debris slap for near-surface nuclear bursts.

UNCLASSIFIED

SECURITY CLASSIFICATION OF THIS PAGE(When Data Entered)

PREFACE

The assistance of Cyrus Knowles and Jack Whitener of R & D Associates in setting up of the matrix of calculations and in obtaining the experimental and calculational data is gratefully acknowledged. Capt. Jerry Stockton of the Strategic Structures Division, Defense Nuclear Agency was the Contracting Officers Representative.

ACCESSION for	
NTIS	White Section <input checked="" type="checkbox"/>
DDC	B.M. Section <input type="checkbox"/>
UNANNOUNCED	<input type="checkbox"/>
J.S. FEB 1977	<input type="checkbox"/>
BY	
DISTRIBUTION/AVAILABILITY NOTES	
SEAL	
A	

TABLE OF CONTENTS

	page
1. INTRODUCTION	3
1.1 Background.	3
1.2 Objectives of the Current Study	3
1.3 Approach.	7
1.4 Conclusions	9
2. BASELINE CALCULATIONS	11
3. BASES FOR JUDGING EFFECTS OF PARAMETRIC CHANGES . .	16
3.1 Time-of-Arrival vs Depth Sensitivity Factor, Σ .	16
3.2 Effective Equivalent Kinetic Energy, E_{eff} , and Effective Energy Ratio, E_{eff}/E_{tot}	18
4. RESULTS OF 1-D CALCULATIONS.	21
4.1 Flyer Plate Parameters.	21
4.1.1 Impact Velocity	21
4.1.2 Density and Flyer Plate Equation of State	25
4.1.3 Internal Energy in Flyer Plate.	29
4.2 Granite Block Parameters.	36
4.2.1 Different Granite EOS Models.	36
4.2.2 Variations within Pyatt EOS	40
4.2.3 Effects of EOS Model Under Other Conditions.	45
4.2.4 Preheating of Granite Block	46
4.3 Numerical Parameters.	47
4.3.1 Zone Size	47
4.3.2 Artificial Viscosity.	48
4.3.3 Energy Iteration.	48
5. DIFFERENCES IN EQUIVALENT KINETIC ENERGY BETWEEN EXPERIMENTAL DATA AND 2-D AND 1-D CALCULATIONS . .	51
APPENDIX A - A SIMPLE INTERPRETATION OF THE HUSKY PUP TIME-OF-ARRIVAL DATA	55
APPENDIX B - THE GRANITE EQUATION OF STATE MODELS FOR TEMPERATURES BETWEEN 0.5EV and 1 KEV	61
REFERENCES.	77

SECTION 1

INTRODUCTION

1.1 Background

The HUSKY PUP underground nuclear test included an experiment in which a curved flyer plate consisting of a sandwich of high and low density materials was accelerated by the nuclear explosion and impacted onto the face of an 8-ft diameter cylinder of granite located 30 cm from the center of the source (Figure 1).

Prior to the test, 2-D radiation-hydro code calculations of the event were performed*, with the intent of evaluating the ability of current numerical techniques to predict the dynamics of acceleration of bomb fragments or debris, and their subsequent impact on the ground in a near-surface nuclear burst. The basis of this evaluation was to be comparisons of calculated characteristics of the shock wave in the granite block (times of arrival, peak pressure, and waveforms vs distance into the block) with measurements of these quantities obtained from the HUSKY PUP experiment.

Figure 2 shows the comparison of the calculated and measured times of arrival (TOA) vs depth in the granite block. Unfortunately, the attempts to measure peak pressures and waveforms were not successful. However, the attenuation of peak pressure with depth in the block can be inferred from the experimental TOA data and from the equation of state models. This interpretation of the data is given in Appendix A.

1.2 Objectives of the Current Study

Despite some fairly substantial differences between the 2-D hydrocode techniques and models (Lagrangian vs Eulerian grids,

* These calculations were made by Lilley at LASL¹, Bailey at Systems, Science, and Software², and Schlaug at Science Applications, Inc.³.

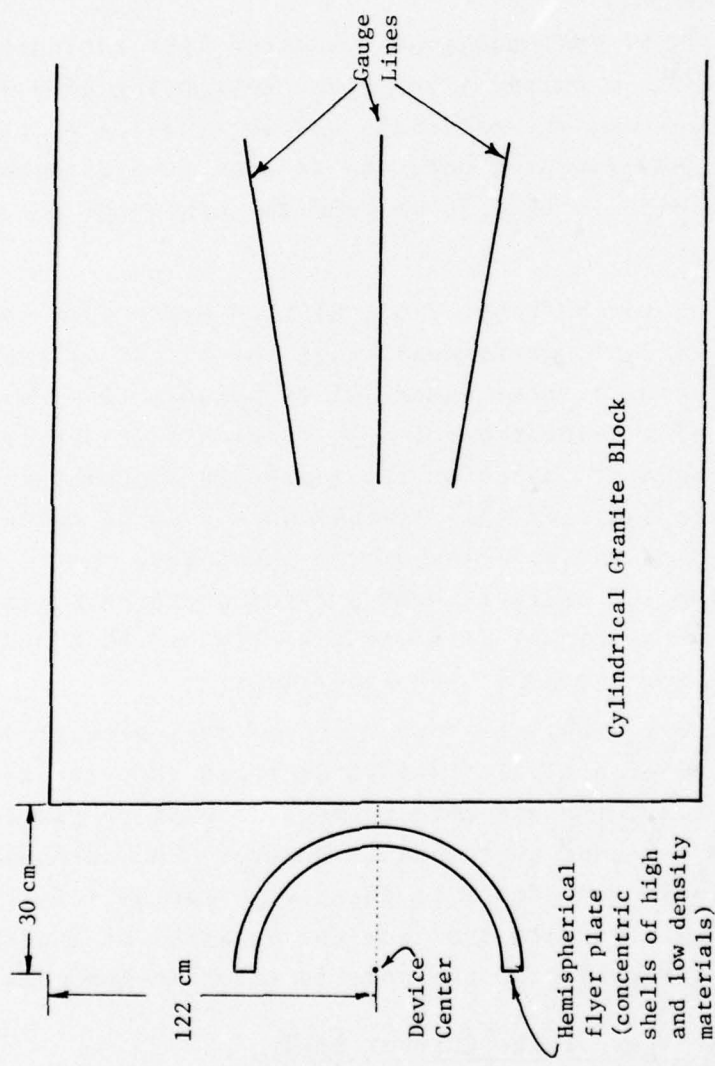


Figure 1. Schematic of HUSKY PUP Granite Block Experiment and Geometry of 2-D Calculations^{1,2,3}

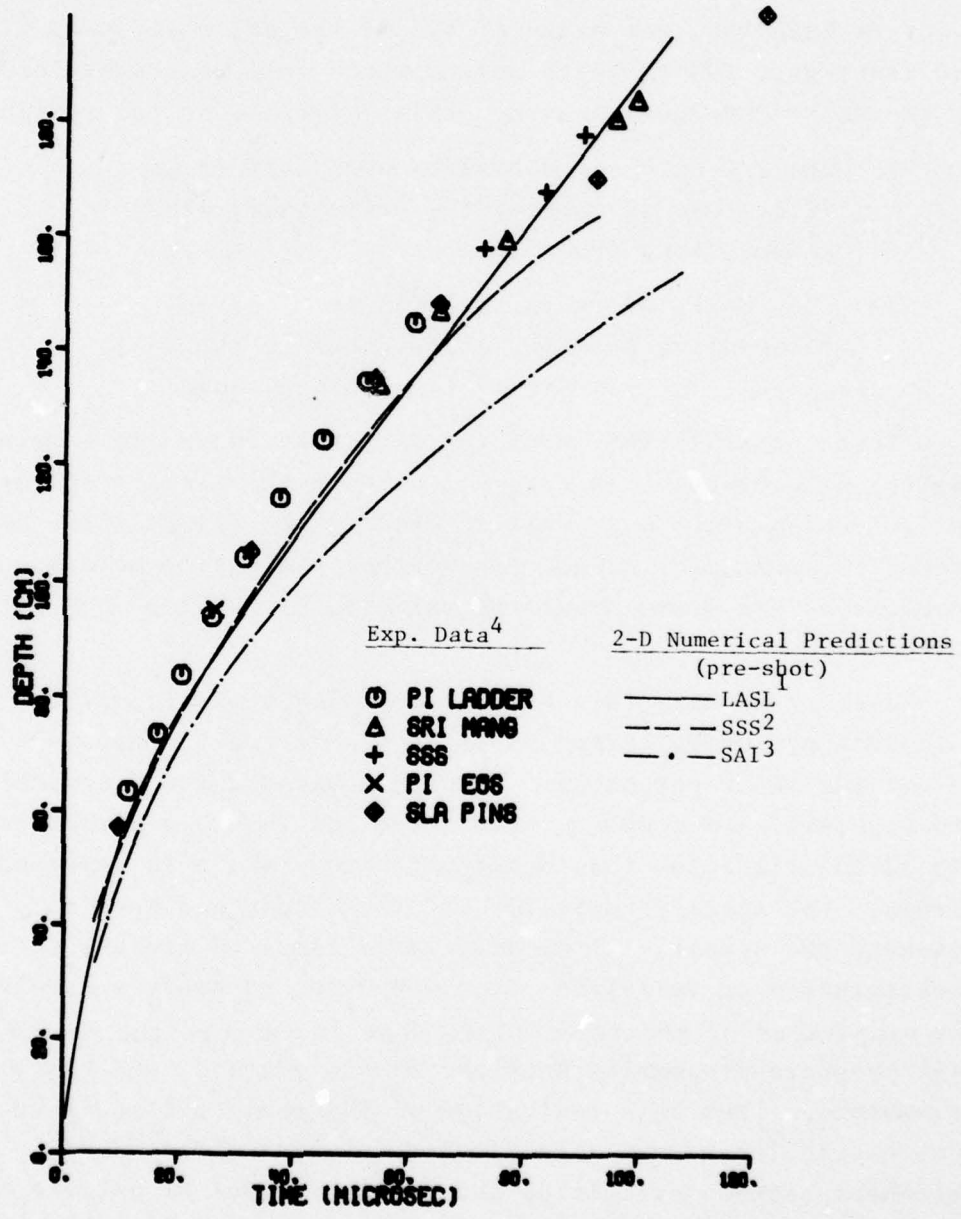


Figure 2. Experimental Time of Arrival Data Compared with the Values Obtained in Preshot 2-D Calculations.

Pyatt vs LASL EOS, for example), two of the calculations (S^3 and LASL) gave TOA vs depth curves which fall reasonably close to the HUSKY PUP measurements. This could be for two reasons:

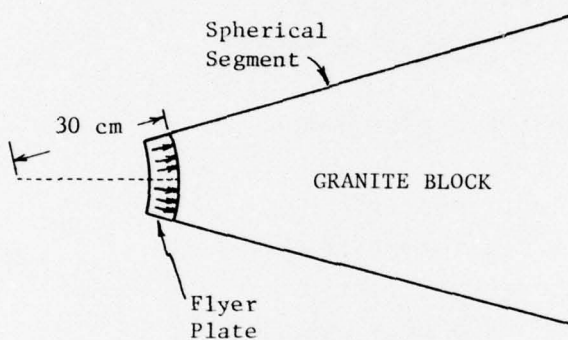
1. The 2-D calculated results were fortuitous (i.e., one or more of the calculators made compensating errors).
2. The TOA vs depth in the granite block is insensitive to major differences in the basic assumptions and calculational techniques.

These possibilities, plus the fact that there are some consistent discrepancies in Figure 2 between the results of the various calculations, as well as between the calculations and the measurements, indicate a need for further evaluation before any conclusions are drawn about the validity of the 2-D code calculations.

One way to make this evaluation would be to repeat the 2-D calculations several times so as to assess their sensitivity to various input parameters. However, because 2-D calculations are expensive and complex, it was decided to use a series of 1-D calculations for the sensitivity study which is reported herein. The specific objective of this study has been to evaluate the sensitivity of calculated times of arrival to uncertainties or variations in a number of parameters involving the properties of the flyer plate when it impacts the granite, the high pressure properties ascribed to the granite, and the numerical parameters. From this evaluation of TOA sensitivity, it becomes possible to judge the significance (or lack thereof) of agreement between calculated and measured times of arrival in the granite block.

1.3 Approach

The calculations were all made using CRALE-1, a 1-D arbitrary-Lagrangian-Eulerian finite difference code. The test geometry was modeled as a 1-D spherical system with the granite block face at a radius of 30 cm.



The flyer plate was assumed to be a uniform material. All of the calculations were started at the instant of flyer plate impact on the granite; flyer plate acceleration by the nuclear burst was not treated.

A baseline set of conditions was first analyzed which gave a TOA vs depth curve that follows the experimental data with good-fidelity, especially considering the 1-D nature of the analysis (See Section 2). For each of the other cases analyzed, the TOA vs depth curve was compared against the baseline curve. The difference, expressed as a sensitivity factor, was used as a measure of the change in the calculated results due to the parameter under consideration. Table 1 summarizes the principal variables which were incorporated into the study. A synopsis (originally prepared by the first author while at RDA) of the eight EOS models investigated in this study appears in Appendix B.

TABLE 1
SUMMARY OF PARAMETERS IN THE 1-D CALCULATIONS

• FLYER PLATE VARIABLES

Uniform Impact Velocity

(40, 45, 47.5, 50, 60 cm/sec)

Velocity Gradients in Plate

(40 to 60, 35 to 65, -40 to 70)

Plate Density

(1.325, 2.65, 5.3 g/cm³)

Internal Energy

(~0, 100, 300, 500, 1450 Mb-cc/gm)

Equation of State for Plate

(Pyatt, Schuster, Tillotson)

• EQUATION OF STATE MODELS FOR GRANITE

Pyatt

Green-1, -2, -3

Kalitkin

LASL

Schuster

Tillotson

• OTHER GRANITE BLOCK AND EOS VARIABLES

Calculated Pressure Level

Release Paths

Preheating by Radiation

EOS Interpolation Method

• NUMERICAL VARIABLES

Zoning

Artificial Viscosity

Energy Iteration Method

1.4 Conclusions

The major conclusions are:

1. The most important parameter in the calculations of the HUSKY PUP granite block experiment (and presumably, therefore, in debris slap from a nuclear burst) is the total energy of the impacting mass. The distribution between kinetic and internal is of secondary importance; internal energy is about 3/4 as effective as kinetic in driving the initial shock into the block.
2. Over a wide variation of material models, the maximum differences in the close-in ($P > 1 \text{ Mb}$) arrival times due to the various EOS models for the flyer plate and granite are equivalent to a change of only 30% in the initial energy of the plate. Since the resultant motions in the granite block should scale approximately as the cube-root of the energy, this difference is small. Hence, the simplest reasonable material model should suffice to calculate the high pressure properties.
3. The difficulties in obtaining experimental data (especially waveforms) in the extreme pressure regime of the granite block in the HUSKY PUP test, and the apparent insensitivity of calculational results to input assumptions in this regime, suggest that future efforts for code validation should emphasize comparisons with test data taken in lower pressure (below 1 Mb) regimes, where material properties may be more significant.

If the correlation between the TOA sensitivity factor, Σ , (as defined in Section 3) and total energy obtained in this 1-D study is extended to the 2-D calculations, an additional conclusion may be inferred:

4. The LASL, S^3 , and SAI calculations differ from the experiment by 18, 23, and 64% in effective energy. Thus the LASL and S^3 results are probably within the uncertainty limits of the HUSKY PUP source yield. Further refinements of those calculations, in order to better match the experimental data, do not, therefore appear to be necessary or fruitful. We conclude that the technology represented by these 2-D calculations is adequate to predict debris slap motions in cratering and ground motion analyses. The substantially lower equivalent energy in the SAI 2-D results is not readily explainable by differences in models, techniques, or assumptions. This suggests the possibility of a calculational error of some sort.

SECTION 2

BASELINE CALCULATION

The baseline set of conditions for the 1-D analyses was as follows:

EOS (for both flyer plate and granite block) - Pyatt

Flyer plate material - granite

Initial density (for both flyer plate and granite block) = 2.65 g/cm^3

Flyer plate velocity = $50 \text{ cm}/\mu\text{sec}$ (uniform)

Flyer plate thickness = 2.0 cm

Internal energy - flyer plate = $.005 \text{ Mb-cc/gm}^*$
granite block = $.0001 \text{ Mb-cc/gm}$

The thickness of the flyer was chosen such that its areal density would be the same as in the concentric flyer in the experiment. The uniform initial velocity of the flyer was chosen to give a total kinetic energy roughly equivalent to that seen in preliminary calculations of the experiment by S³.

The flyer was resolved by 5 cells of equal thickness (0.4 cm). The cells in the granite block increased by 0.25% per cell from an initial thickness of 0.4 cm (at the flyer-block interface). At a radius of 210 cm (180 cm into the block, the end of the region of interest), the cells were about 0.9 cm thick.

The TOA vs depth curve obtained using the baseline conditions is shown in Figure 3**, along with the experimental data and with the results of the 2-D calculations. While the baseline

* $1 \text{ Mb-cc/gm} = 10^{12} \text{ ergs/gm}$

** Incremental methods, like finite difference codes, do not provide a smooth TOA curve, but rather a series of discrete points corresponding to the shock arrival at each cell. The smooth curves shown throughout this report are least-square fits of the form $D = at^b$ of the discrete points calculated between 60 cm and 180 cm depth in the granite.

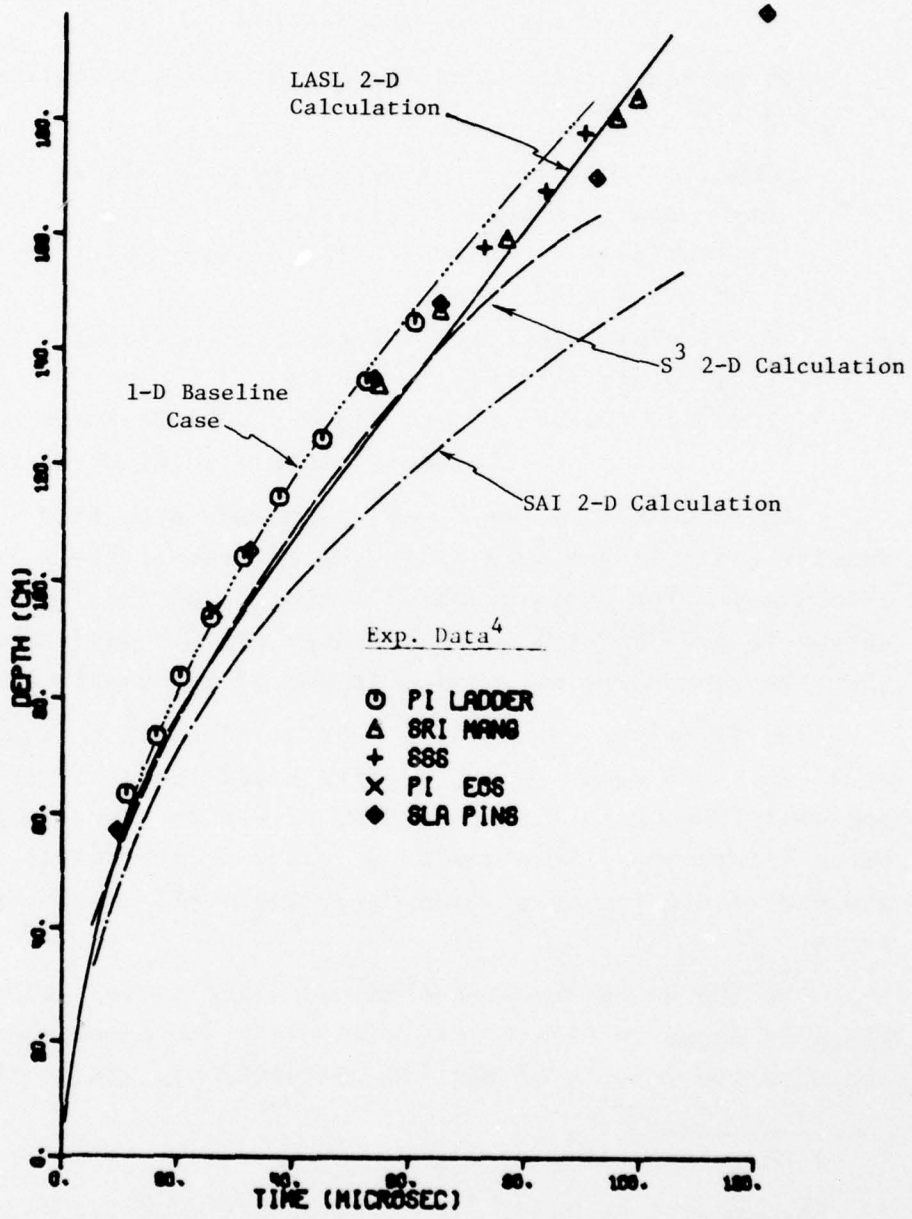


Figure 3. Comparison of the Times of Arrival for the 1-D Baseline Case, the 2-D Pre-shot Calculations and the HUSKY PUP Experiment.

calculation was not intended to exactly match the test conditions, it was gratifying to obtain the good correspondence shown in Figure 3. This correspondence helps to establish the relevance of the baseline conditions to the objectives of the study and also shows that 1-D simulation of the experiment is quite realistic. There is an increasing discrepancy between the calculated and measured TOA, with the measured TOA being about 10% later than the calculated TOA by 180 cm depth. This presumably reflects the 2-D attenuation effects (e.g. lateral relief) which would be expected to appear at late times in the experiment.

Figure 4 shows the stress, velocity, and displacement time histories calculated in the Baseline Case at a representative depth (95 cm) in the granite block. Figure 5 is a plot of the peak pressure vs depth. The knee at about 60 cm depth is caused by a strong second pulse. This pulse arises when the rear of the flyer plate converges and rebounds from the center of the 1-D spherically symmetric geometry of the problem. Such a secondary pulse may not be present in the actual test geometry.

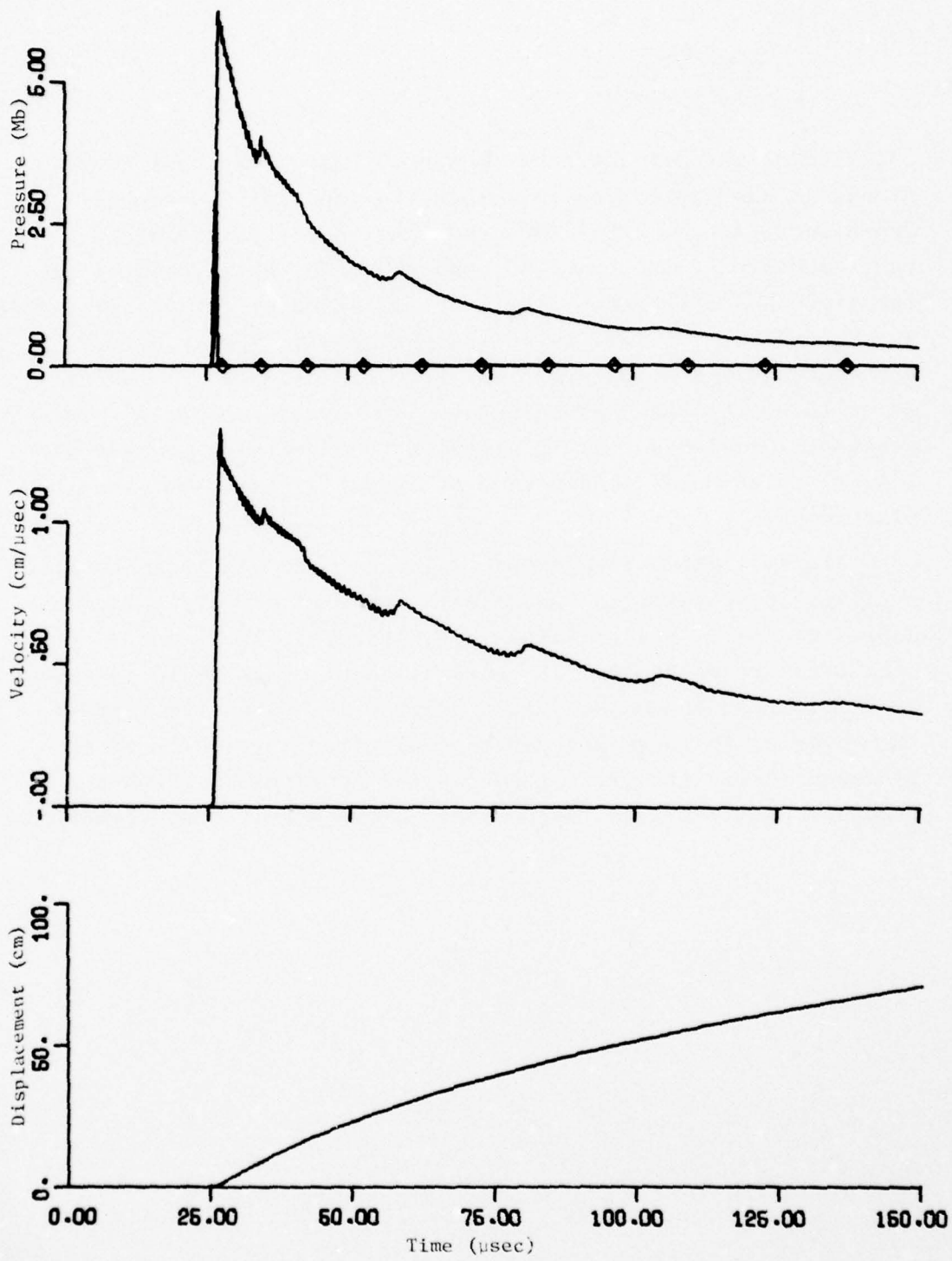


Figure 4. Stress, Velocity, and Displacement Histories in Baseline Case
at 95 cm Depth in Granite Block.

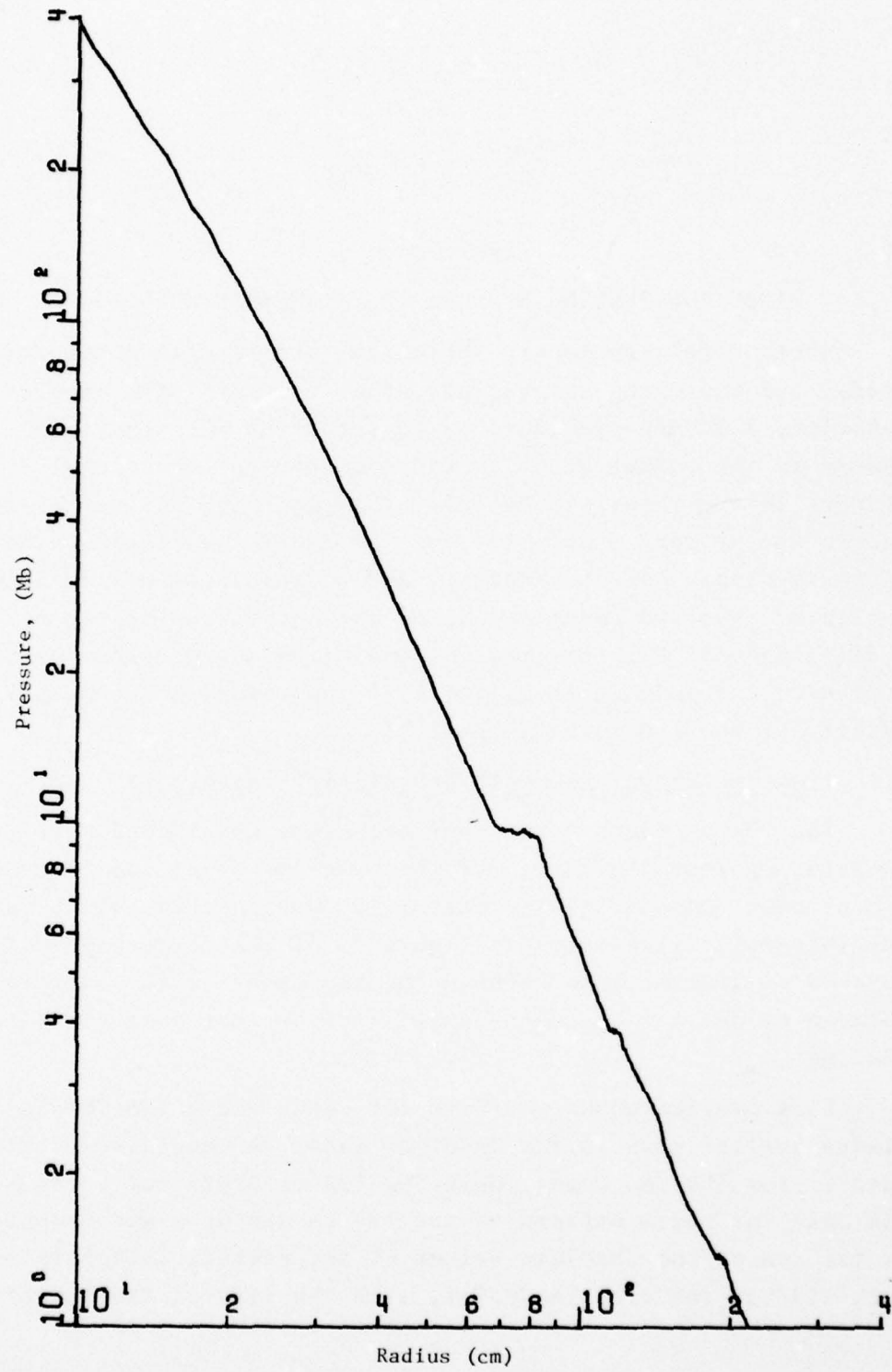


Figure 5. Peak Pressure in the Granite Block vs Radius from Device Center for the Baseline Case.

SECTION 3

BASES FOR JUDGING EFFECTS OF PARAMETRIC CHANGES

Where single-parameter variations are made in a sensitivity study, and where the meaningful output consists of a single quantity, a common procedure is to determine the fractional change in the output quantity as a function of fractional changes in the input parameters. This approach was not practical in the present study, inasmuch as the TOA vs depth curve is not a simple output quantity, and because some of the input variables involved combinations of parameters and/or overall model changes. For this reason, the criteria described below were used for judging the effects of input variables on the results of the 1-D calculations.

3.1 Time-of-Arrival vs Depth Sensitivity Factor (Σ)

The TOA vs depth curves for each case considered were compared against the curve for the baseline case, and a non-dimensional TOA sensitivity factor, Σ , was calculated. Σ is the integral, illustrated in Figure 6, of the *percentage difference* in arrival time between the two cases in the interval between 60 and 180 cm depth, normalized by that interval (i.e., 120 cm).

Σ is considered as positive for cases where the TOA is always earlier than in the Baseline Case, and negative if always later. For the few cases where the TOA vs depth curve crossed the baseline curve between 60 and 180 cm depth, Σ was computed as the sum of the absolute values of the partial integrals on each side of the crossing point, with the sign of the larger.

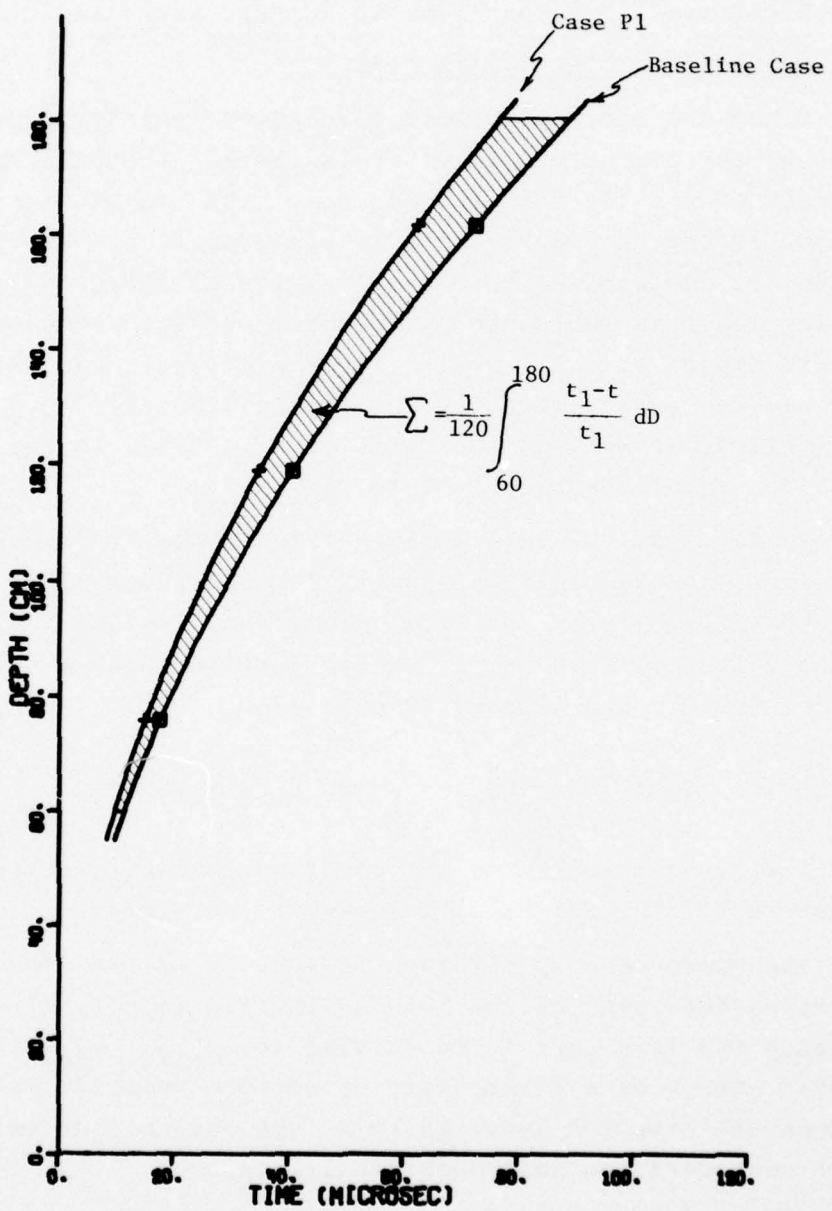


Figure 6. TOA vs. Depth for Baseline Case and Case P1, Illustrating the Definition of the Sensitivity Factor, Σ .

3.2 Effective Equivalent Kinetic Energy, E_{eff} , and Effective Energy Ratio, E_{eff}/E_{tot}

Since the shock propagation velocity is directly determined by the impact velocity, it is obvious that the impact velocity of the flyer plate, and hence its kinetic energy, has a major effect on TOA vs depth in the granite block. For this reason, it was decided to relate results of those cases involving *other* variables to the results obtained when only the uniform impact velocity of the flyer plate was changed. In this way, an effective equivalent kinetic energy, E_{eff} , could be obtained, as well as the ratio of this value to the total actual energy in the flyer plate, E_{eff}/E_{tot} .

To do this, the relationship between the TOA sensitivity factor, Σ , and the energy (essentially all kinetic) of uniform-velocity flyer plates was first derived by fitting a quadratic to the values of Σ and E_{tot} for the Baseline Case ($V=50$ cm/ μ sec), Case P1 ($V=40$), and Case P2 ($V=60$), i.e.,

$$\Sigma = -.3227 E_{tot}^2 + 1.119 E_{tot} - .7964 \quad (1)$$

Eqn. 1 will be referred to as the standard $\Sigma-E_{tot}$ curve for uniform-velocity, all-kinetic-energy flyer plates.

The value of E_{eff} for each subsequent run was obtained by inserting the value of the TOA sensitivity factor, Σ , calculated for each run into Eqn. 1 and solving for E_{eff} . E_{eff} is thus the kinetic energy of a flyer plate of uniform velocity which will produce the same TOA sensitivity as the variable or variables under consideration in a specific 1-D case.

Figure 7 graphically illustrates the determination and use of E_{eff} . This is a plot of the TOA sensitivity factor, Σ , vs total energy, E_{tot} (normalized by the total energy of the Baseline Case). The solid curve in Eqn. 1, represents the standard relationship between Σ and E_{tot} when the plate velocity is uniform and virtually all energy in the plate is initially kinetic. As an example of how results of 1-D cases are related to Eqn. 1, the calculated value of Σ , and E_{tot} are plotted for Case P7. Its total energy, E_{tot} , is 79.1% of the Baseline Case, but it produces the same effect on the TOA sensitivity factor, Σ , as a uniform-velocity plate having 72.3% of the energy of the Baseline Case. Thus the effective equivalent kinetic energy, E_{eff} for the P7 flyer plate is .723, and its effective energy ratio, E_{eff}/E_{tot} , is $.723/.791 = .915$. E_{eff}/E_{tot} is seen graphically in Figure 7 to be merely a measure of the horizontal distance between the plotted value of Σ and E_{tot} for any case and the standard curve (Eqn. 1).

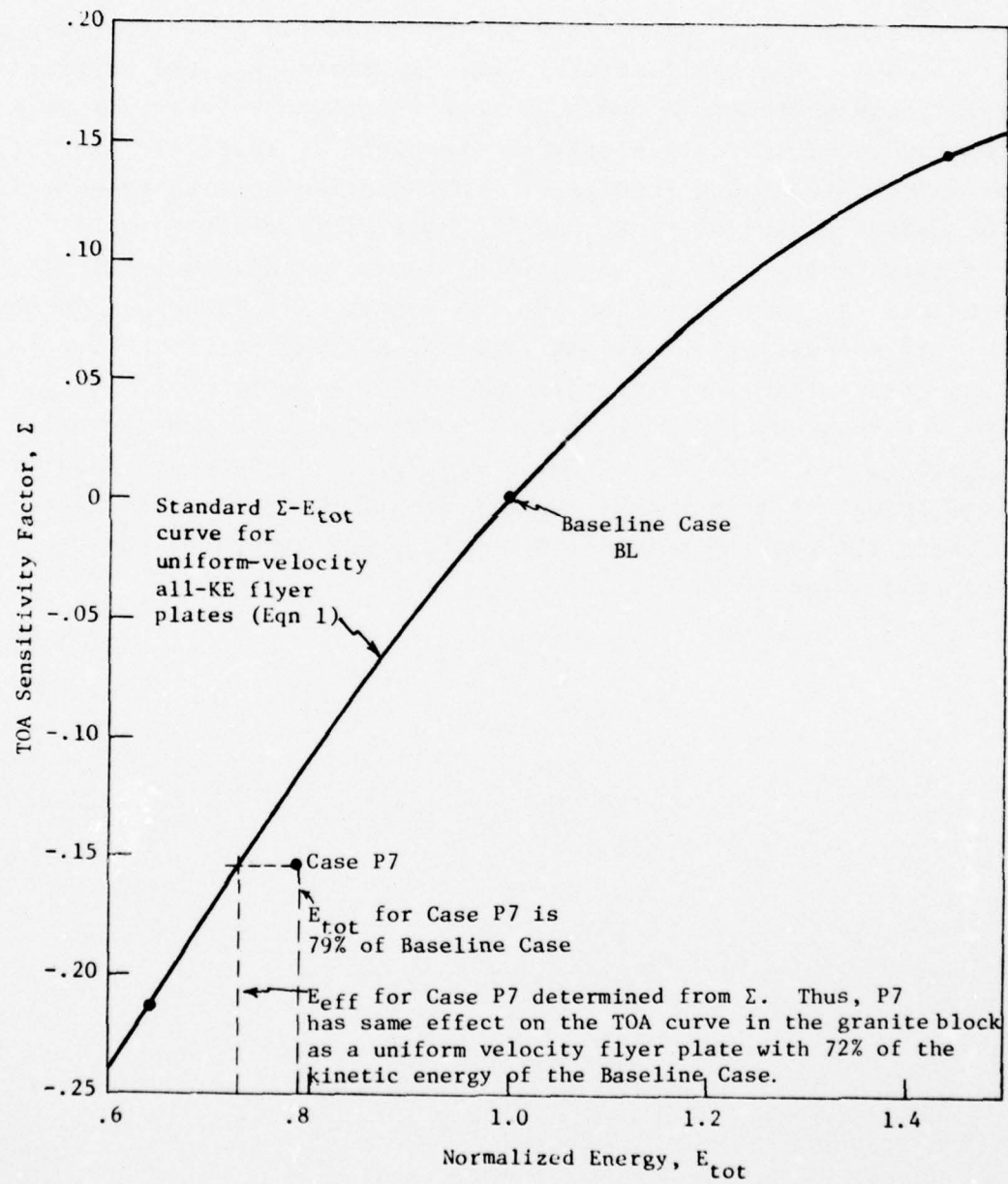


Figure 7. Illustration of Effective Equivalent Kinetic Energy, E_{eff} .

SECTION 4

RESULTS OF 1-D CALCULATIONS

The 38 one-dimensional (spherical symmetry) cases analyzed in this study are listed in Table 2. They are grouped into four general categories according to whether the parameter being examined was associated primarily with the flyer plate (the P-cases), granite equation of state model (E), other granite block and EOS variables (B), or computational technique (C).

Table 2 summarizes the most important results of the study, including the TOA sensitivity factor (Σ), the equivalent effective kinetic energy, E_{eff} , and the effective energy ratio, $E_{\text{eff}}/E_{\text{tot}}$, as defined in Section 3.

4.1 Flyer Plate Parameters

4.1.1 Impact Velocity

Initially, the simplest and most obvious parameter to vary was the impact velocity of the flyer plate on the granite block. In cases BL, P1, P2, P3, and P4, the velocities within the plates were uniform. These velocities were varied from 40 cm/ μ sec to 60 cm/ μ sec. The TOA vs depth for these cases is shown in Figure 8. As expected, increasing the impact velocity produces a consistent decrease in the TOA at a given depth.

Since the actual flyer plate velocity was probably not uniform through the plate, three problems (Cases P5, P6, and P7) were run in which the velocity increased linearly with radius within the plate. Thus in Case P5, the front (impacting) surface of the plate was traveling at 65 cm/ μ sec, while the rear was at 35 cm/ μ sec, with linear variation in between. In Case P7, the front surface was at 70 cm/ μ sec, while the rear surface was moving at -40 cm/ μ sec (i.e., it was converging back towards the source). This roughly approximates a velocity profile calculated

TABLE 2. SUMMARY OF 1-D CASES AND RESULTS

Case No.	Primary Variable	Plate Velocity (cm/usec)	Kinetic Energy (Normalized to Baseline Energy)	TOA Sensitivity Factor, Σ	Equivalent KE, E_{eff}	Effective Energy Ratio E_{eff}/E_{tot}	Apparent Equivalence of IE to KE
Baseline (BL)	Pyatt EOS, $V=50$ $\rho_o = 2.65$ (granite), IE _o = 0	50	1.0	-0	0	1.0	-
P1	Uniform velocity	60	1.4396	-0	.146	1.0	-
P2	Uniform velocity	40	.6403	-0	-.212	1.0	-
P3	Uniform velocity	45	.8100	~0	-.092	.826	1.02
P4	Uniform velocity	47.5	.9025	-0	-.051	.899	.996
P5	Ramp velocity	40/60	1.0920	-0	.031	1.068	.978
P6	Ramp velocity	35/65	1.1523	-0	.053	1.121	.973
P7	Ramp velocity	-40/70	.7911	-0	-.155	.724	.915
P8	Density, $\rho_o = 5.3$	50	1.0358	-0	.014	1.031	.995
P9	Density, $\rho_o = 1.325$	50	.9944	~0	-.013	.973	.978
P10	Density, $\rho_o = 1.325$	45	.8055	-0	-.016	.804	.998
P11	Int. Energy,	50	1.0	.0843	.023	1.051	.969
	IE = 100 Mb-cc/gm					.60	
P12	IE _o = 500	50	1.0	.4216	.115	1.306	.919
P13	IE _o = 1450, V=0	0	0	1.2235	-.046	.909	.743
P14	IE _o = 100, Ramp vel	-40/70	.7911	.0843	-.116	.787	.899
P15	IE _o = 300, Ramp vel	-40/70	.7911	.2530	-.045	.909	.871
P16	IE _o = 500, Ramp vel	-40/70	.7911	.4216	.015*	1.032	.851
P17	Same as P16, with Cavity pressure = 3 Mb	-40/70	.7911	.4216	.013*	1.027	.847
P18	Same as P16, with Schuster EOS	-40/70	.7911	.4216	.035	1.078	.889
P19	Tillotson EOS	50	1.0	0	.001*	1.0	-
P20	Tillotson EOS, expanded tungsten plate ($\rho_o = 2.65$), IE _o = 100	50	1.0	.0843	.031	1.058	.985

TABLE 2. (Con't) SUMMARY OF 1-D CASES AND RESULTS

Case No.	Primary Variable	Plate Velocity (cm/ μ sec)	Kinetic Energy (Normalized to Baseline Energy)	Internal Energy (Normalized to Baseline Energy)	TOA Sensitivity Factor, Σ	Equivalent KE, E_{eff}	Effective Energy Ratio E_{eff}/E_{tot}	Apparent Equivalence of IE to KE	
								KE, E_{eff}	Effective Energy Ratio E_{eff}/E_{tot}
GRANTTE EOS MODELS									
E2	Green-1 EOS	50	1.0	0	.007	1.186	1.186		
E3	Green-2	50	1.0	0	.094	1.237	1.237		
E4	Green-3	50	1.0	0	.012*	1.026	1.026		
E5	Kalitkin	50	1.0	0	.021	1.046	1.046		
E6	LASL	50	1.0	0	.080	1.195	1.195		
E6A	LASL, $IE_O = 500$, ramp vel	-40/70	.7911	.4216	.092	1.231	1.015		
E6B	LASL, $V=40$	40	.6403	0	-.101	.811	1.267		
E7	Schuster	50	1.0	0	.094	1.237	1.237		
E8	Tillotson	50	1.0	0	.114	1.304	1.304		
B1	P=1.2P (Pyatt EOS)	50	1.0	0	.008	1.017	1.017		
B2	P=0.8P (Pyatt EOS)	50	1.0	0	-.023	.953	.953		
B3	γ -law unloading	50	1.0	0	-.007	.986	.986		
B4	Preheat, 0.2 Mb-cc/gm	50	1.0	.0872	.024	1.053	.963	.61	
B5	Preheat, 20 Mb-cc/gm	50	1.0	.4302	.115	1.307	.914	.71	
B6	Simple interpolation in Pyatt EOS table	50	1.0	0	-.005	.990	.990		
OTHER VARIATIONS									
C1	Half-size zones	50.66	1.0266	0	.011	1.024	.997		
C2	Reduce Viscosity	50	1.0	0	.004*	1.009	1.009		
C3	No P-e iteration	50	1.0	0	-.004*	.992	.992		
NUMERICAL PARAMETERS									

* TOA Curve crossed Baseline Curve. Σ equals the sum of the magnitudes of the integrals above and below the baseline, with the sign of the larger.

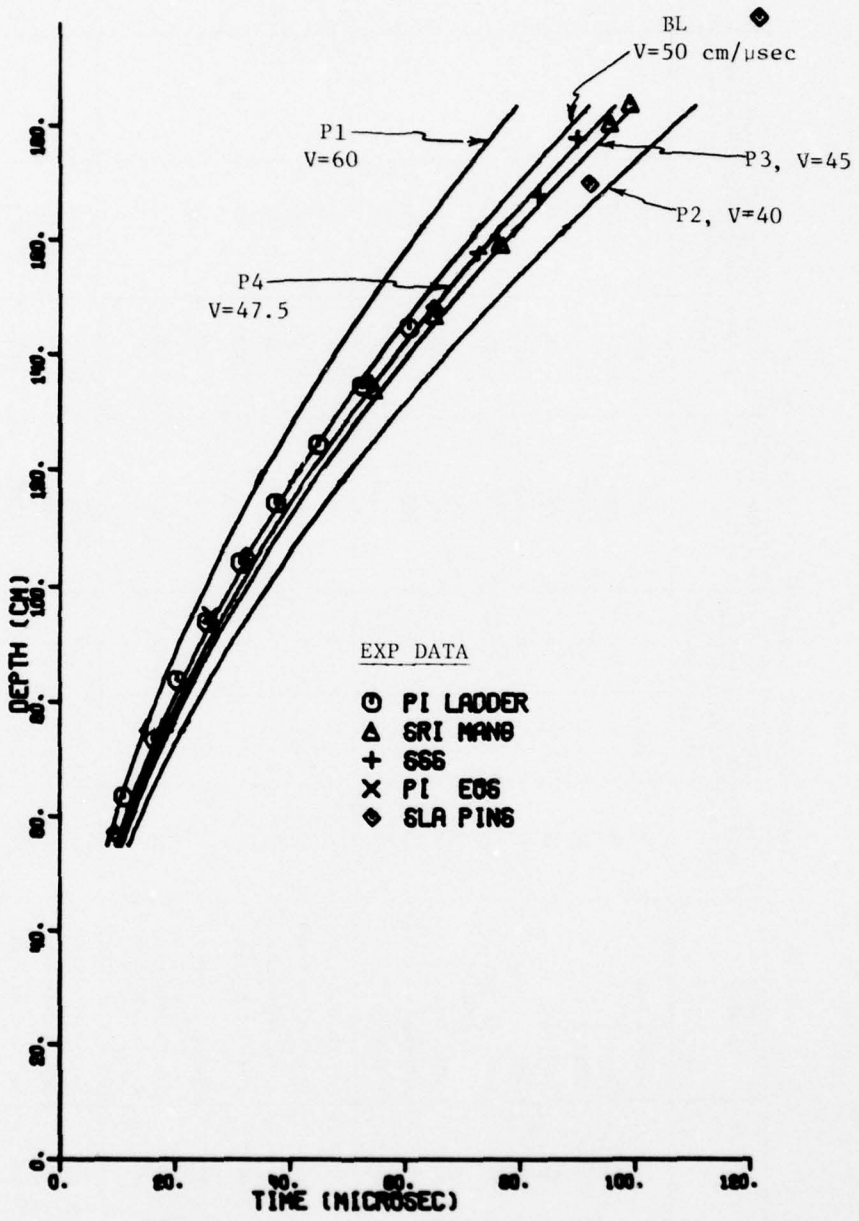


Figure 8. Variation of Time of Arrival with the Velocity of the Flyer Plate. HUSKY PUP Experimental Data are Included for Comparison.

by S^3 in a preliminary 2-D study. TOA results of these cases are compared with the Baseline Case in Figure 9.

Figure 10 shows the results of all of these cases on the ΣE_{tot} plane, and compares them with the standard ΣE_{tot} relationship (Eqn. 1). The three non-uniform velocity cases, P5, P6, and P7, fall only slightly below the curve (i.e., the TOA are generally later) indicating that when the kinetic energy is *non-uniformly* distributed in the flyer plate, its effect on the TOA in the granite plate is less by a small amount than an equivalent energy *uniformly* distributed in the plate. This is somewhat surprising in Case P7, since part of the kinetic energy in that case was directed away from the granite block. Even so, the effective energy ratio, E_{eff}/E_{tot} , for Case P7 is .915, which says that the strongly non-uniform nature of the P7 flyer plate resulted in a loss of effectiveness of only 8.5%, as compared to a uniform-velocity flyer plate. This suggests that the total kinetic energy in the flyer plate has a much more important effect on the TOA vs depth in the granite block than the detailed distribution of the kinetic energy within the flyer plate.

4.1.2 Density and Flyer Plate Equation of State

The second flyer plate parameter studied was its density. The pre-test plate consisted of sandwich layers of high and low density materials. At the time of impact with the granite block the actual flyer plate had presumably undergone several stages of compression and rarefaction due to the force of the explosion, and its density profile was clearly uncertain. In the Baseline Case, the flyer plate was granite with a uniform density of $\rho_0 = 2.65 \text{ g/cm}^3$. In Cases P8 and P9, ρ_0 was increased and decreased by a factor of 2, to 5.3 and 1.325 g/cm^3 . The effects of these changes on TOA vs depth in the granite block are seen in Figure 11 to be quite small.

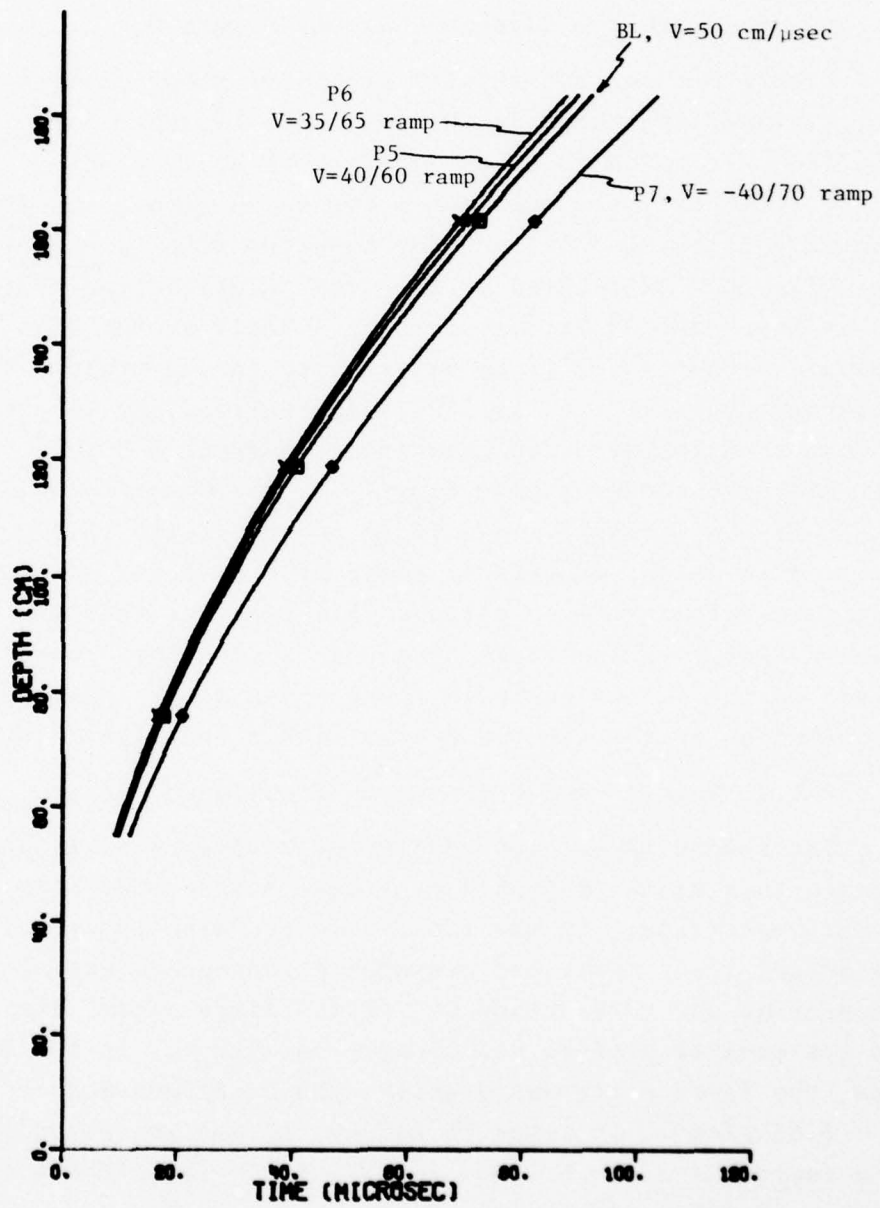


Figure 9. Variations of Time of Arrival for Non-uniform Velocity Flyer Plates.

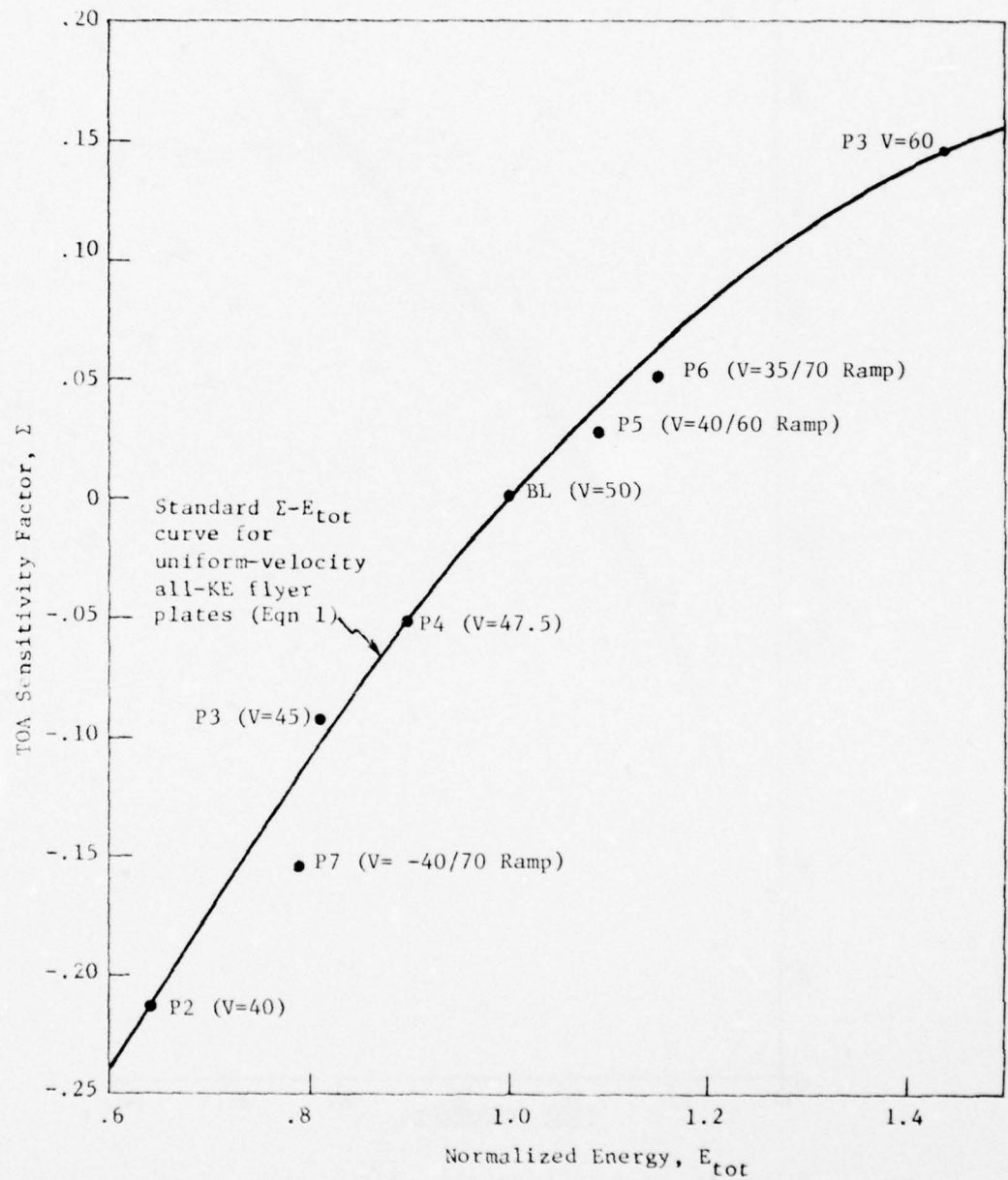


Figure 10. TOA Sensitivity Factor, Σ , vs Normalized Total Energy for Cases in Which the Velocity (cm/ μ sec) and its Distribution in the Flyer Plate are Varied.

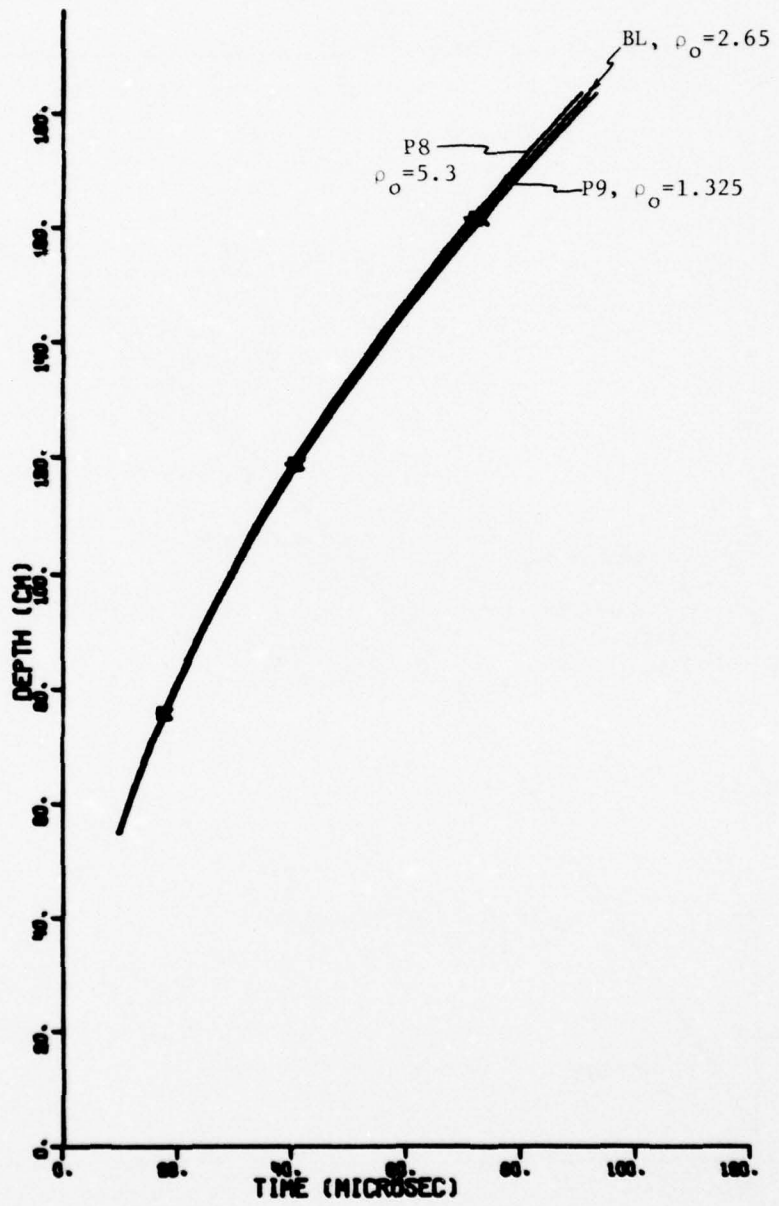


Figure 11. Variations in Time of Arrival Due to Changes
in the Initial Density, ρ_0 , of the Flyer Plate.

Similarly, when the EOS model for the flyer plate was changed from the Pyatt model (used in the Baseline Case) to the Tillotson model (Case P19), the change in TOA vs depth was negligible. Even when the flyer plate was changed to expanded Tungsten ($\rho_0 = 2.65$), and its internal energy, IE_0 , was raised to 100 Mb-cc/gm, (Case P20), the effects on TOA vs depth in the granite block were small. These flyer plate EOS comparisons are shown in Figure 12.

When the TOA sensitivity factor, Σ , and the normalized total energy, E_{tot} , for the flyer plate density and EOS cases are plotted (Figure 13), it is seen that they deviate only slightly from the standard Σ vs E_{tot} relationship (Eqn. 1). The largest deviation is for the low density flyer plate (Case P9, with $\rho=1.325$). For this case the effective energy ratio is still .978, or just 2.2% less effective than a flyer plate of density, $\rho_0 = 2.65 \text{ gm/cm}^3$.

4.1.3 Internal Energy in Flyer Plate

Two sets of cases were run to investigate the effects of the internal energy of the flyer plate on the TOA in the granite block. In the Baseline Case, the initial internal energy, IE_0 , was essentially zero (.005 Mb-cc/gm). In Cases P11 and P12, IE_0 was increased to 100 and 500 Mb-cc/gm, respectively. Since the velocity was held at $V_0 = 50 \text{ cm}/\mu\text{sec}$, these changes in internal energy raised the total energy in Cases P11 and P12 by 8.4% and 42.2%. As might be expected, increasing the flyer plate internal energy shifted the TOA toward earlier arrivals, as seen in Figure 14. However, when the TOA sensitivity factor, Σ , is plotted vs normalized total energy, E_{tot} in Figure 15, it is seen that Cases P11 and P12 fall below the standard Σ vs E_{tot} curve (Eqn. 1) for all-kinetic-energy cases. This indicates

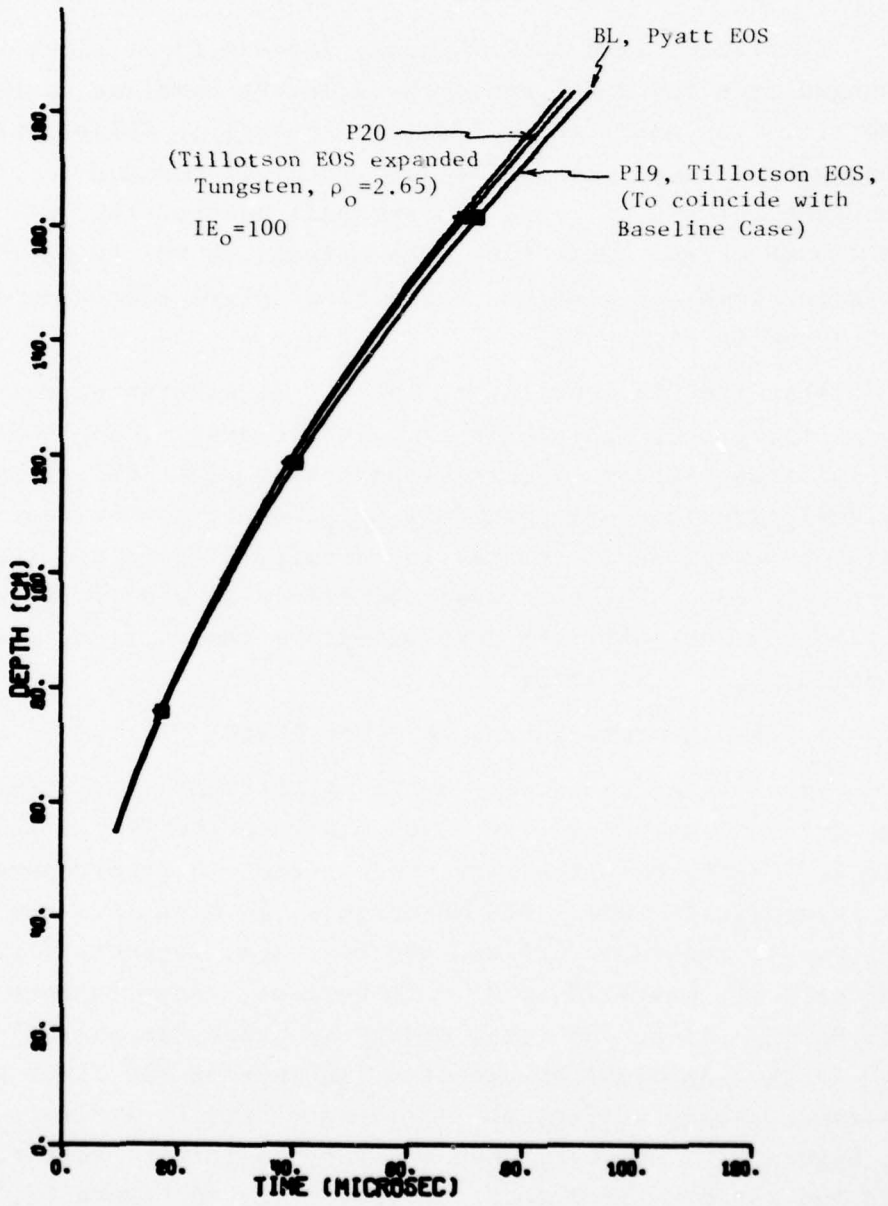


Figure 12. Effect of Different Flyer Plate Equations of State on Times of Arrival.

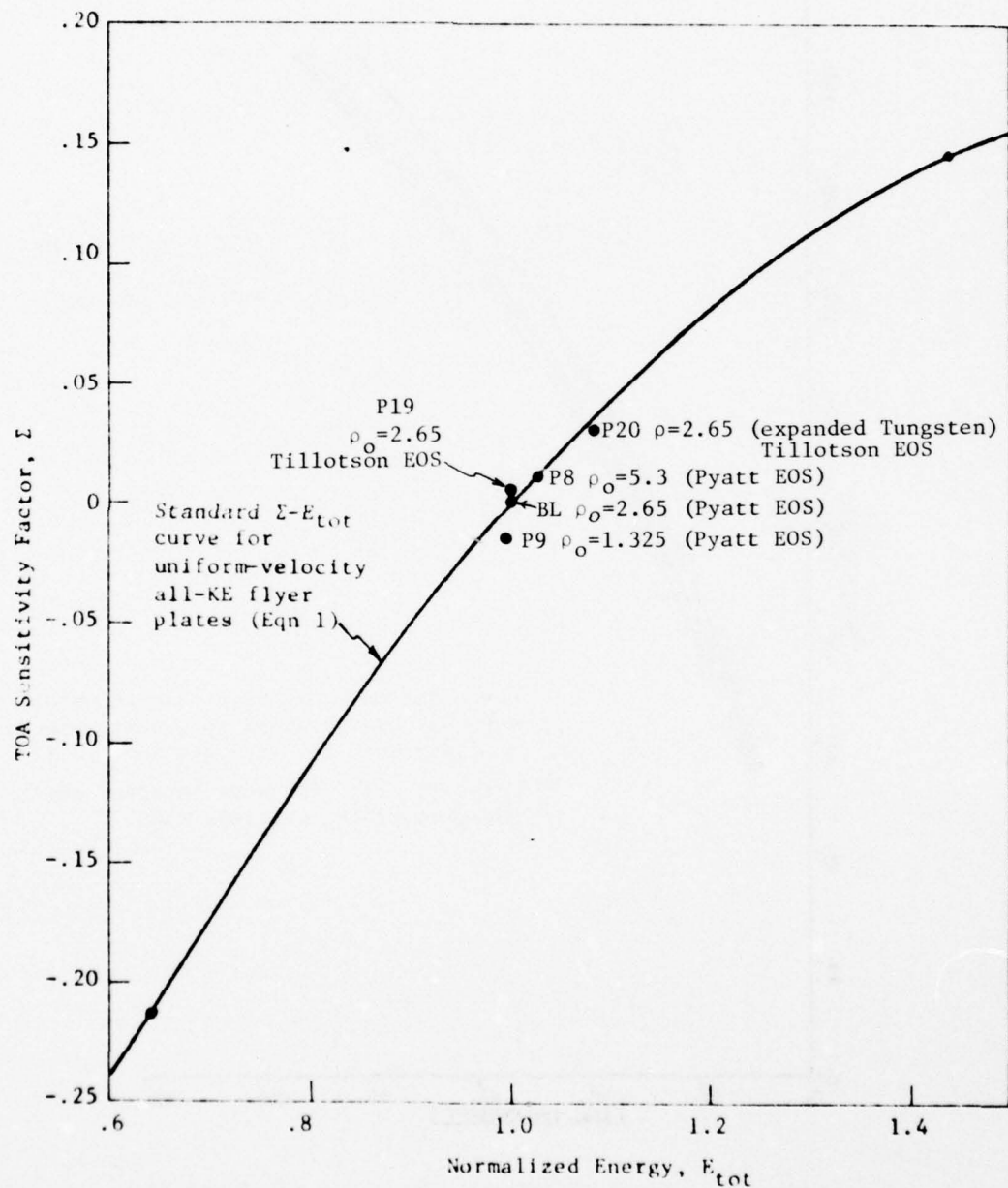


Figure 13. TOS Sensitivity Factor, Σ , vs Normalized Total Energy for Cases in Which the Flyer Plate Density and EOS Model are Varied.

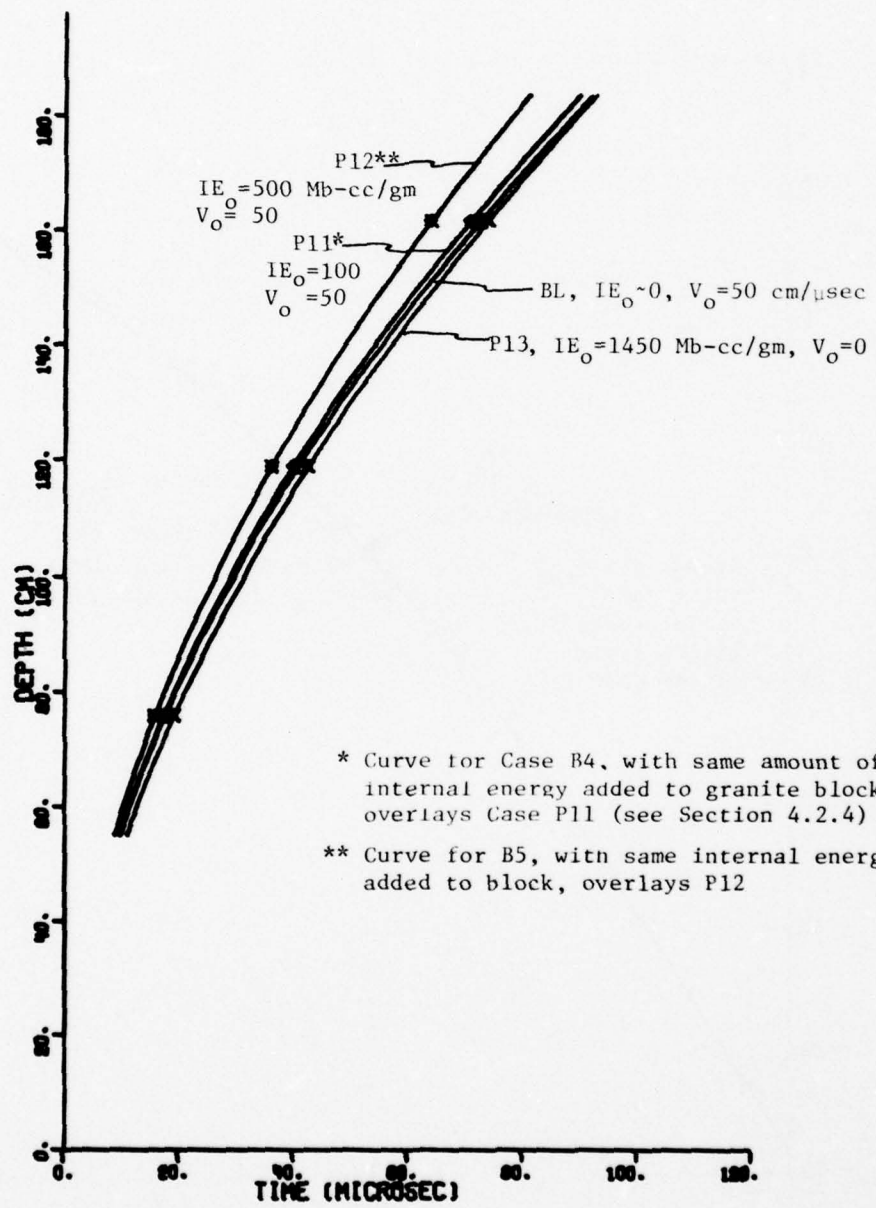


Figure 14. Effect of Internal Energy in the Flyer Plate on Time of Arrival in Granite Block.

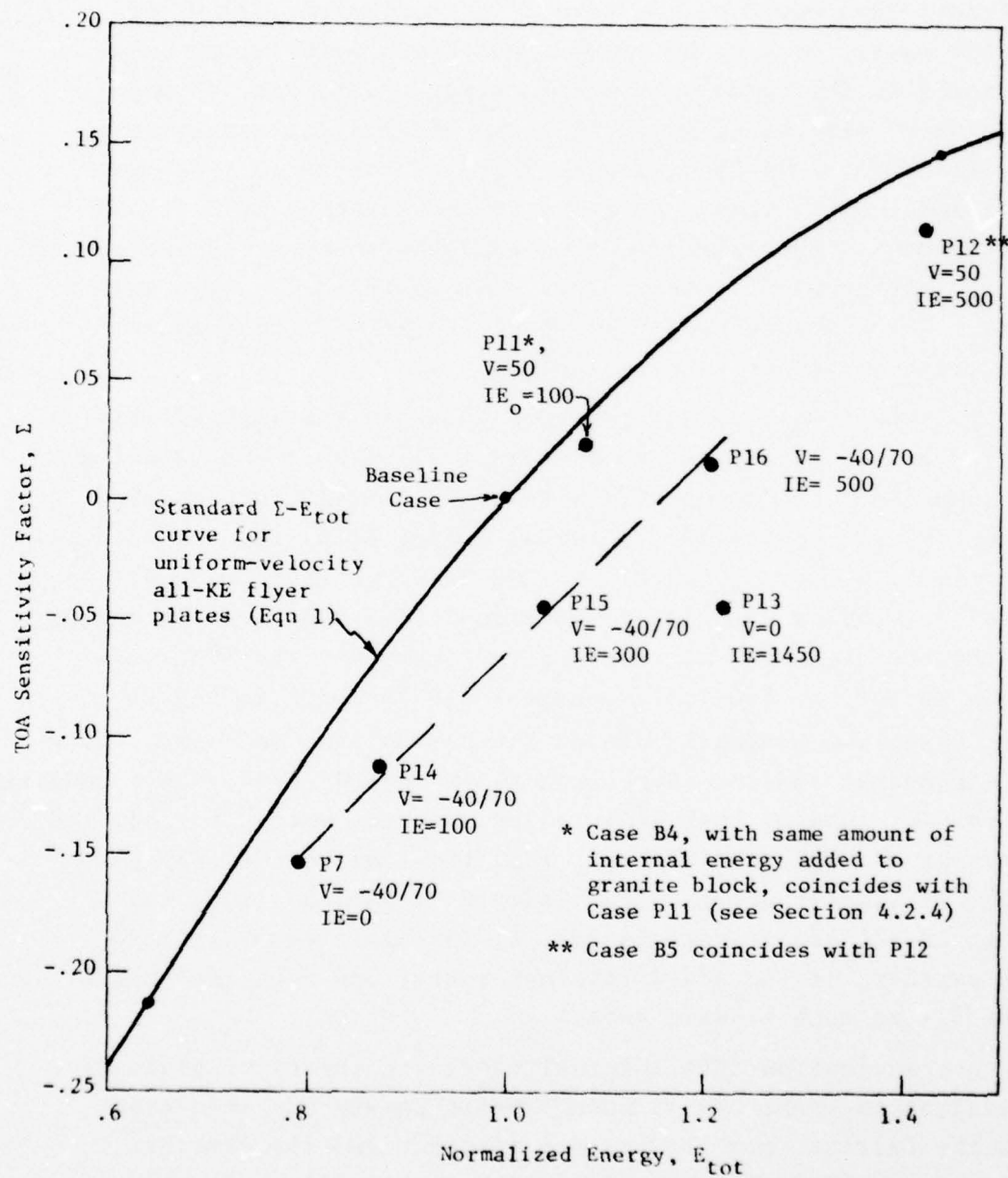


Figure 15. TOA Sensitivity Factor, Σ , vs Normalized Energy for Cases in Which the Internal and Kinetic Energies of the Flyer Plate were Varied. (Velocities in cm/ μ sec, Energy in Mb-cc/gm)

that when *internal* energy is added to the flyer plate, the shock strength produced in the granite is lower, (and hence the TOA is later) than would be the case if an equivalent amount of *kinetic* energy were to be added. More specifically, in Cases P11 and P12, the normalized total energy was raised, through addition of internal energy, to 1.084 and 1.422, respectively. The effective equivalent kinetic energies for these cases was 1.051 and 1.306. Thus increasing internal energy by 8.4% and 42.2% produced the same effect as would be achieved by increasing kinetic energy by 5.1% and 30.6%. Put another way, internal energy in these cases was only about 3/4 as effective as an equivalent amount of kinetic energy.

To see if this effect is independent of the assumed initial kinetic energy level, three additional cases were run in which the same -40 to 70 cm/ μ sec ramp velocity distribution as used in Case P7 was specified. Internal energy densities varied from essential zero (Case P7) to 100 Mb-cc/gm (Case 14), 300 Mb-cc/gm (P15), and 500 Mb-cc/gm (P16). The TOA vs depth curves for these four cases are compared in Figure 16 the TOA sensitivity factor, Σ , and total energies are included in Figure 15. These cases are nominally fit by the dashed line in Figure 15, which has a somewhat smaller slope than the standard curve. This confirms the earlier finding that addition of internal energy to the flyer plate has a smaller effect on Σ than the addition of the same amount of kinetic energy. For Cases P14, P15, and P16, the change in TOA sensitivity factor, Σ , was again equivalent to that expected if the added internal energy had been replaced by about 3/4 as much kinetic energy.

The indication that internal energy in the flyer plate is equivalent to about 3/4 as much kinetic energy was seen even when the initial velocity was set to zero, and the internal energy set to 1450 Mb-cc/gm (Case P13). The TOA vs depth curve is included on Figure 14 and is seen to fall fairly close to the Baseline Case. On the Σ vs E_{tot} plot in Figure 15, Case P13,

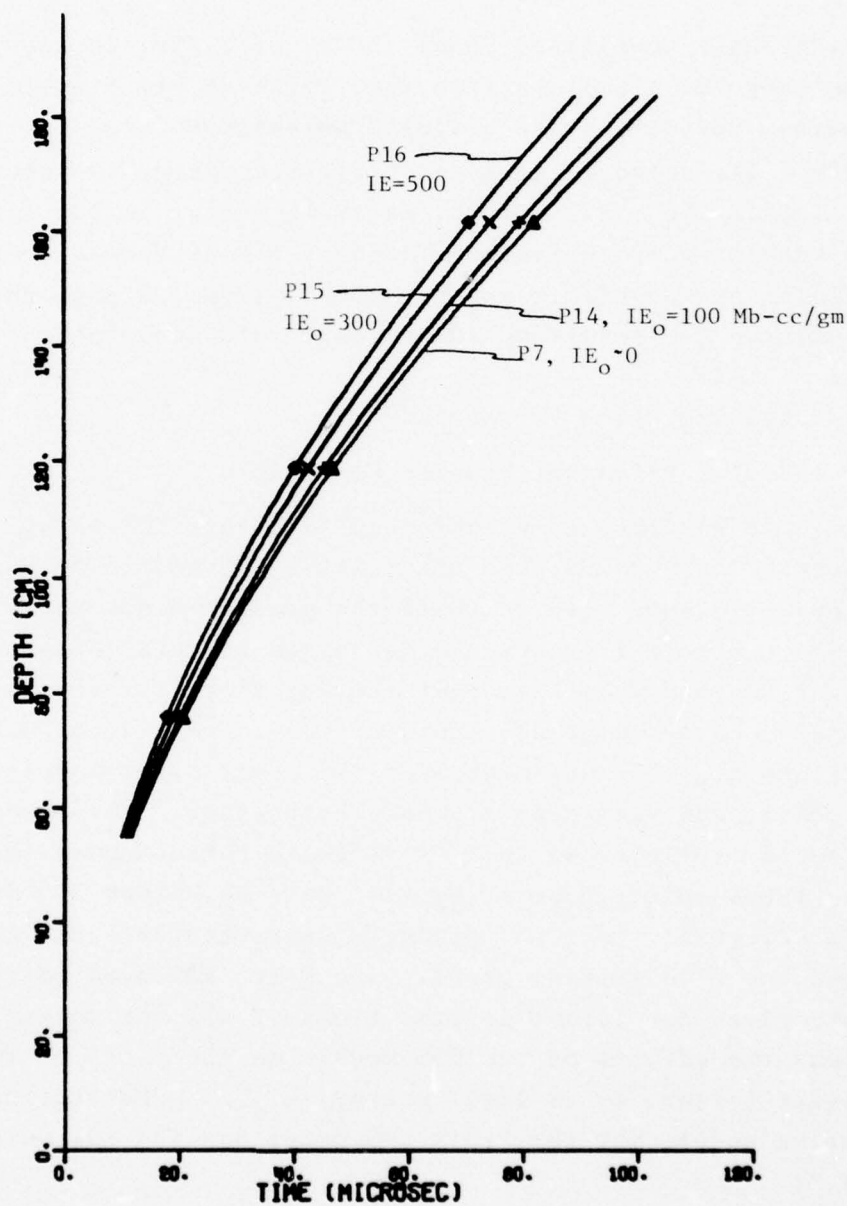


Figure 16. Effect of Internal Energy of Flyer Plates with Non-uniform Velocity Profile on Time of Arrival.
(All Cases, $V = -40/70 \text{ cm}/\mu\text{sec}$ Ramp)

which has a normalized total energy of 1.256, is seen to have the same TOA sensitivity factor, Σ , as an all-kinetic-energy, uniform velocity plate having a normalized total energy of .909. The ratio of equivalent kinetic energy-to-internal energy is $.909/1.256 = .72$. Thus, internal-energy in the flyer plate is consistently equivalent to about 3/4 as much kinetic energy, insofar as the effect on the shock introduced into the granite block and the resulting TOA vs depth are concerned.

4.2 Granite Block Parameters

4.2.1 Different Granite EOS Models

The Baseline Case (BL) used the Pyatt EOS model. In Cases E2 through E8, the alternative EOS models described in Appendix B were used for both the granite block and the flyer plate. Figure 17 shows the Hugoniots calculated for each of the eight EOS models. Note that the Hugoniots for five of the models nearly coincide (LASL, Green-1, Green-2, Schuster, and Tillotson). The Hugoniots for the other three models (Pyatt, Green-3, and Kalitkin) are somewhat softer. This behavior directly reflects in the TOA vs depth curves shown in Figure 18; the three softer models (Pyatt: Case BL, Green-3: Case E4, and Kalitkin: Case E5) produced consistently later arrival times than the five stiffer cases. The Pyatt EOS used in the Baseline Case gives the latest arrival times of all the models. Figure 19 shows the effects of the EOS models on the plots of TOA sensitivity factor, Σ , vs total energy, E_{tot} . Substitution of alternative models for the Pyatt EOS model has the following effects on Σ :

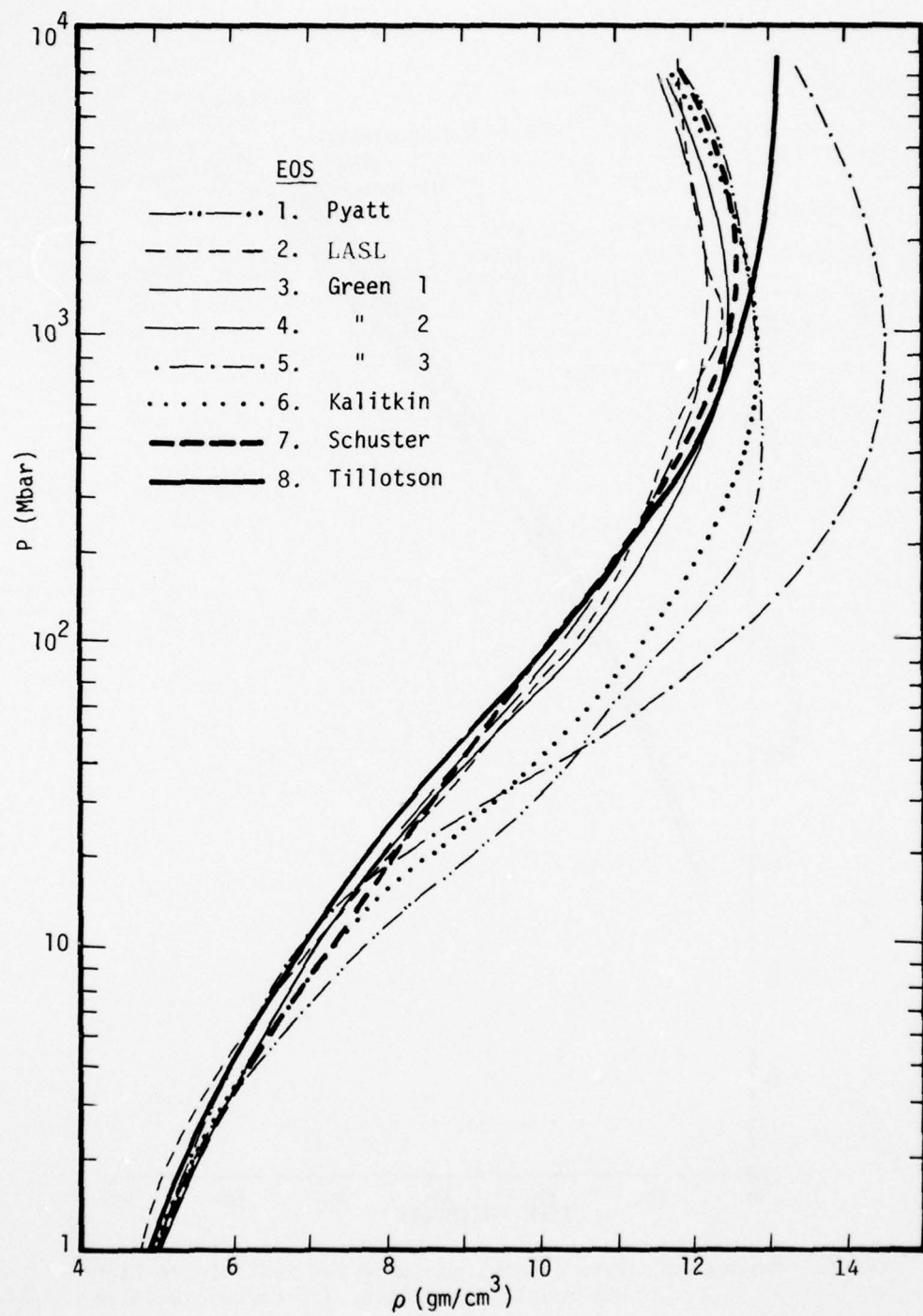


Figure 17. Principal Hugoniots Calculated from the Eight Models for Quartz

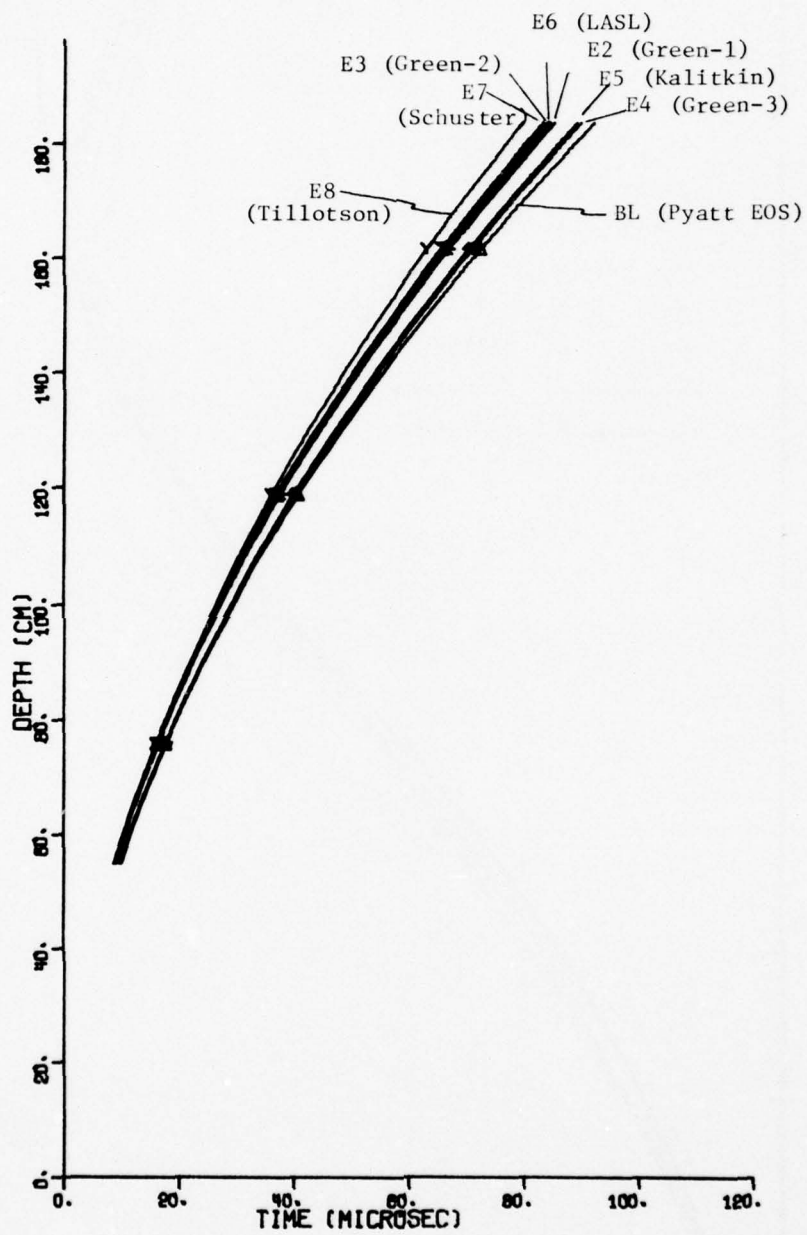


Figure 18. Time of Arrival Curve for Each of the Eight EOS Models of Granite. (50 cm/ μ sec Uniform Velocity Flyer Plate).

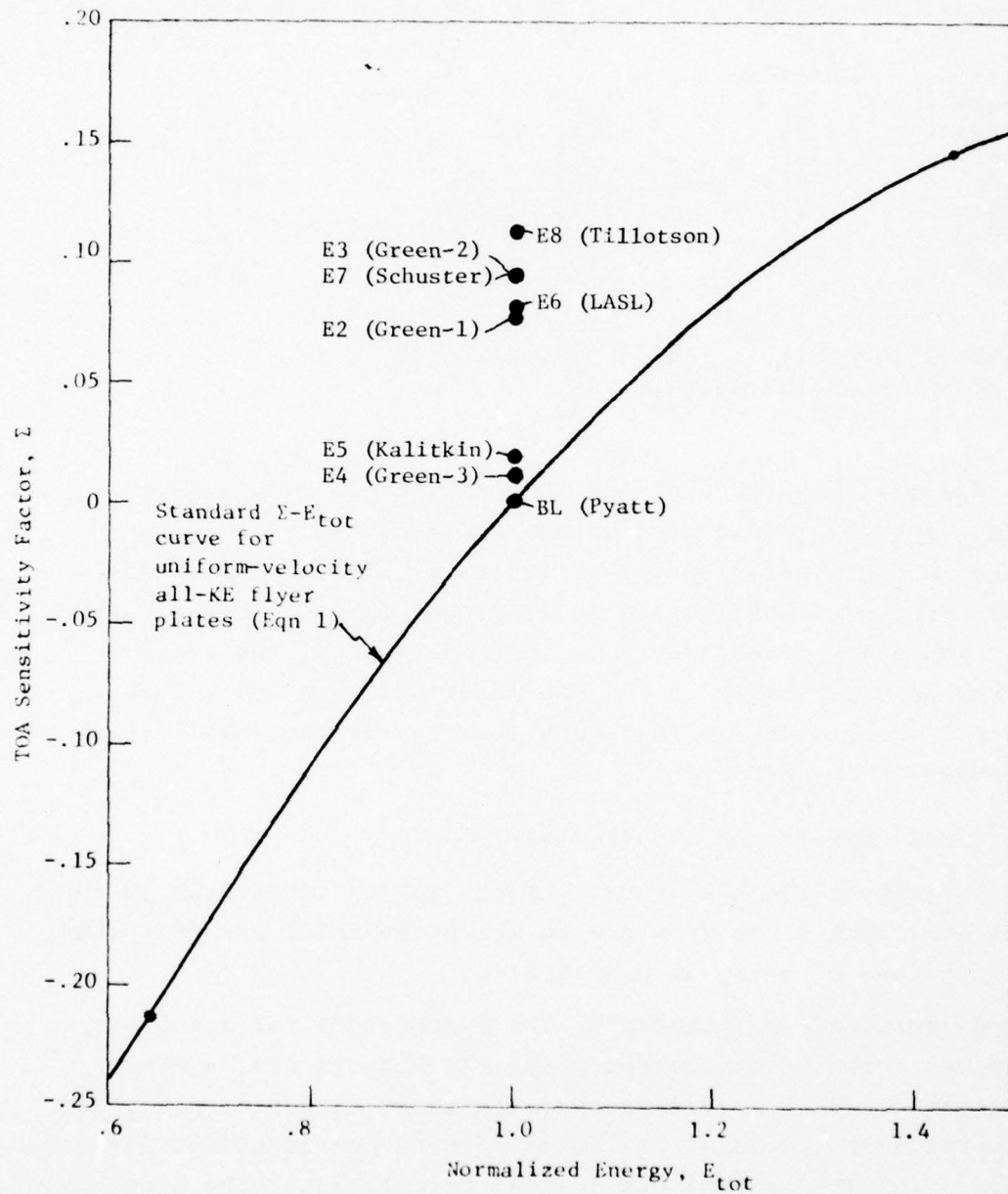


Figure 19. TOA Sensitivity Factor vs Normalized Energy for Cases in which the Equations of State of the Granite Block was Varied.

<u>EOS Model</u>	<u>Case</u>	<u>Effect on Σ</u>	<u>Equivalent Change in KE of flyer which will have same effect on Σ</u>
Pyatt*	Baseline	-	-
Green-3	E4	.012	+ 3%
Kalitkin	E5	.021	+ 4%
Green-1	E2	.077	+18%
LASL**	E6	.080	+19%
Schuster	E7	.094	+24%
Green-2	E3	.094	+24%
Tillotson	E8	.114	+30%

* Used in 2-D calculations by S³ and SAI

**Used in 2-D calculation by LASL

The maximum effect of the EOS model on the TOA Sensitivity Factor (for the models considered) was equivalent to a 30% change in the kinetic energy of the flyer plate. Since subsequent effects of debris slap (e.g. ground motions) are expected to be nominally proportional to the cube-root of the coupled energy, an uncertainty in the EOS model which is equivalent to a 30% uncertainty in the kinetic energy of the debris is probably not important.

4.2.2 Variations within Pyatt EOS

To examine the sensitivity of the TOA to variations in the Pyatt EOS, four cases were run in which the model was perturbed or the method of using it was altered.

As outlined in Appendix B, the Pyatt model for granite is a complex formulation incorporating the Saha theory, a Birch-Murnaghan fit of the zero pressure isotherm, Hugoniot data, and an approximate treatment of the 120-350 kb quartz-stishovite phase change. To expedite its use in code calculations, the model has been reduced to a table look-up form. Rather than reconstruct

the table by varying parameters in the basic formulation, it was felt that the sensitivity of results to the model could be at least crudely determined by arbitrarily changing the pressure given by the table for the conditions in each computational cell and cycle. In Case B1, this pressure was increased by 20%; in Case B2, it was decreased by 20%. The effects on the TOA vs depth curves in Figure 20 are seen to be small. Reducing the pressure (Case B2) had a somewhat larger effect on the TOA than a corresponding increase (Case B1). Effects on the TOA sensitivity factor, Σ , are seen in Figure 21. Reducing the pressure by 20% had an effect equivalent to reducing the flyer plate kinetic energy by 4.7%.

In another change to the Pyatt model, the release adiabats in the model were replaced in Case B3 by a simple γ -law dependence i.e.,

$$P = (\gamma_H - 1)\rho E \quad (2)$$

γ_H in Eqn. 2 was chosen for each calculational zone, based on the Hugoniot pressure experienced. Thus

$$(\gamma_H - 1) = P_H / \rho_H E_H \quad (3)$$

As seen in Figure 22, the γ -law release paths do not reflect the detailed structure of paths calculated with the Pyatt model for shocks in the range below about 10 Mb. Nonetheless, the TOA vs depth curves for Case B3 coincides almost exactly with the Baseline Case in Figure 20.

The final modification to the Pyatt EOS model was to change the method of interpolation between two values in the tables. Normally, the logs of the two quantities are first determined, then linear interpolations are made between logs, then the

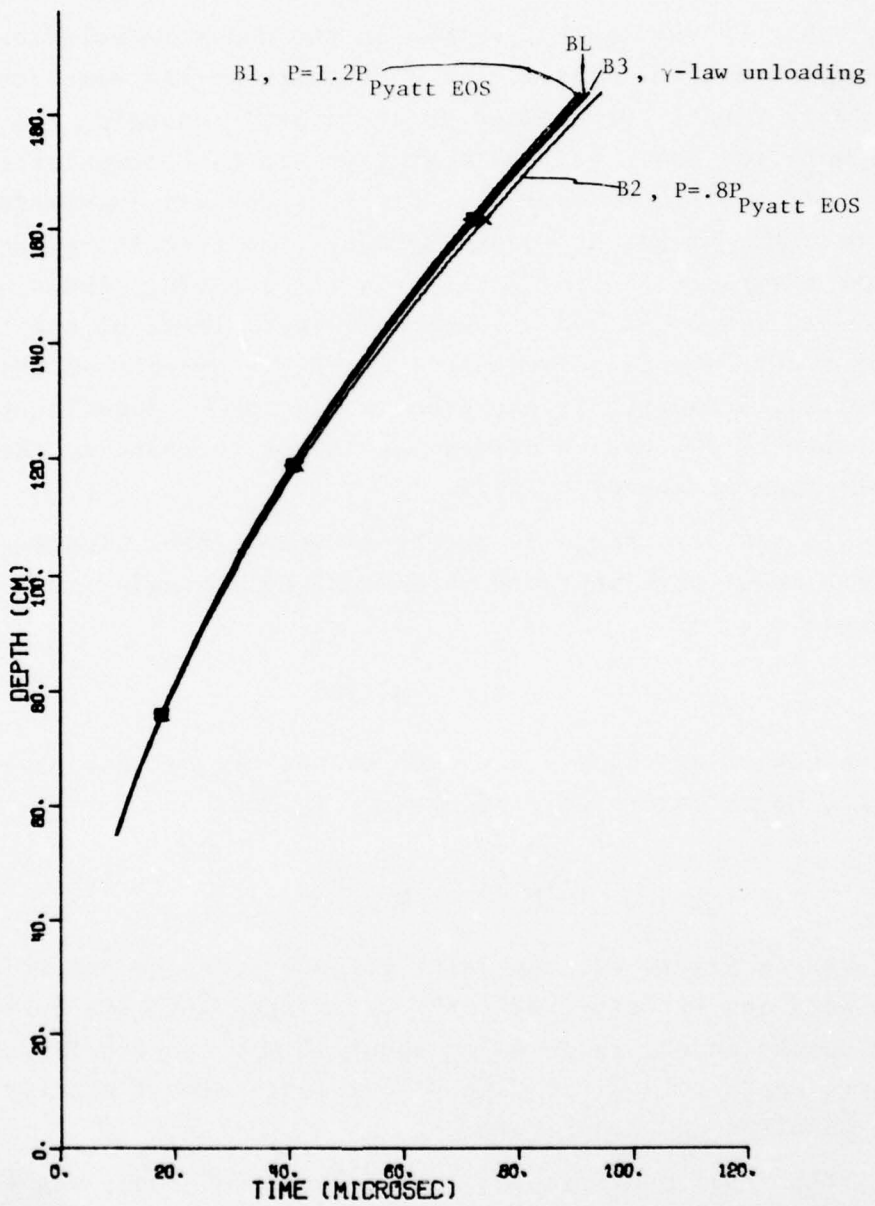


Figure 20. Variations in Time of Arrival Due to Modifications of the Pyatt EOS Model of Granite.

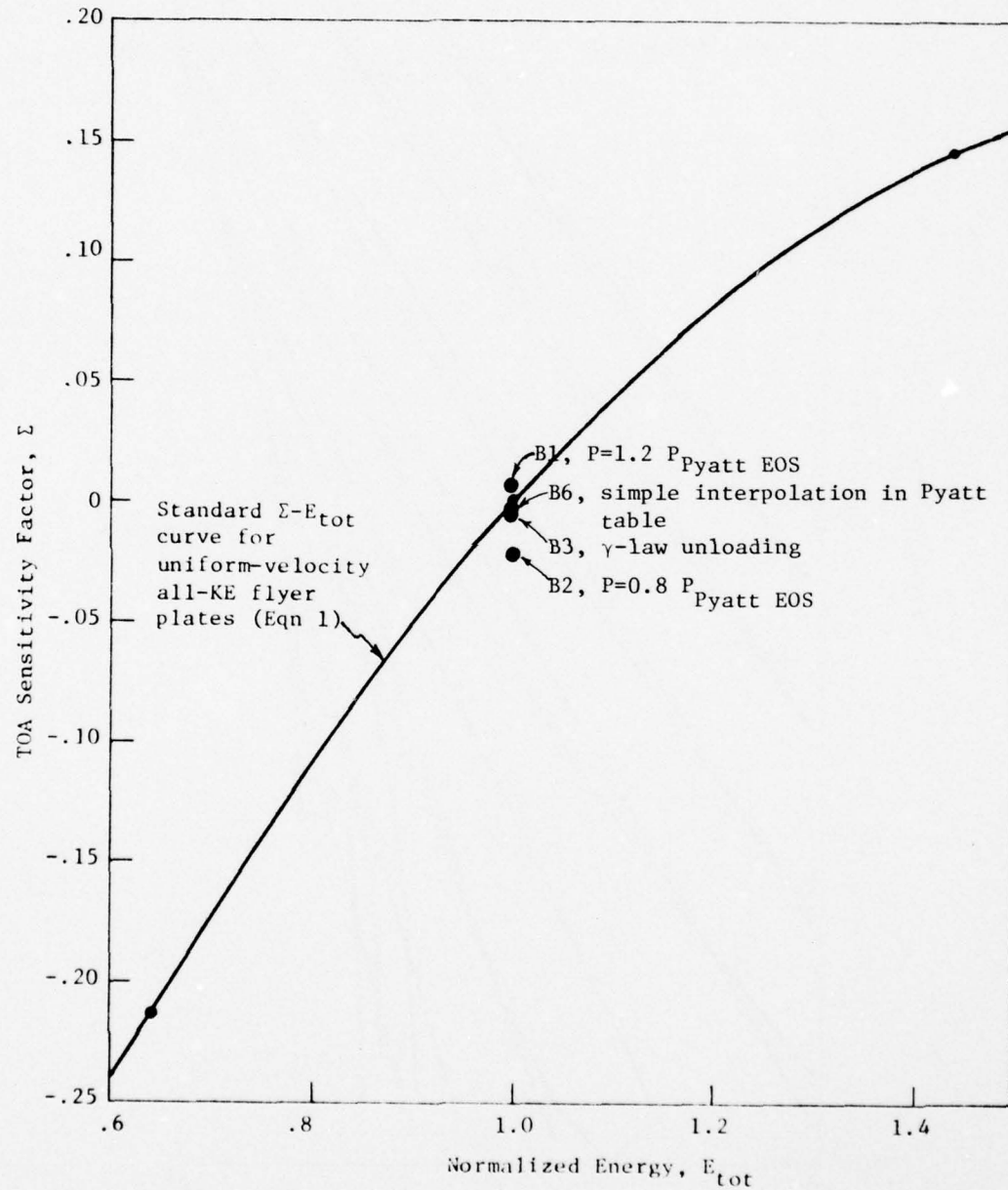


Figure 21. TOA Sensitivity Factor, Σ , vs Normalized Energy for Cases in which the Pyatt EOS was Modified.

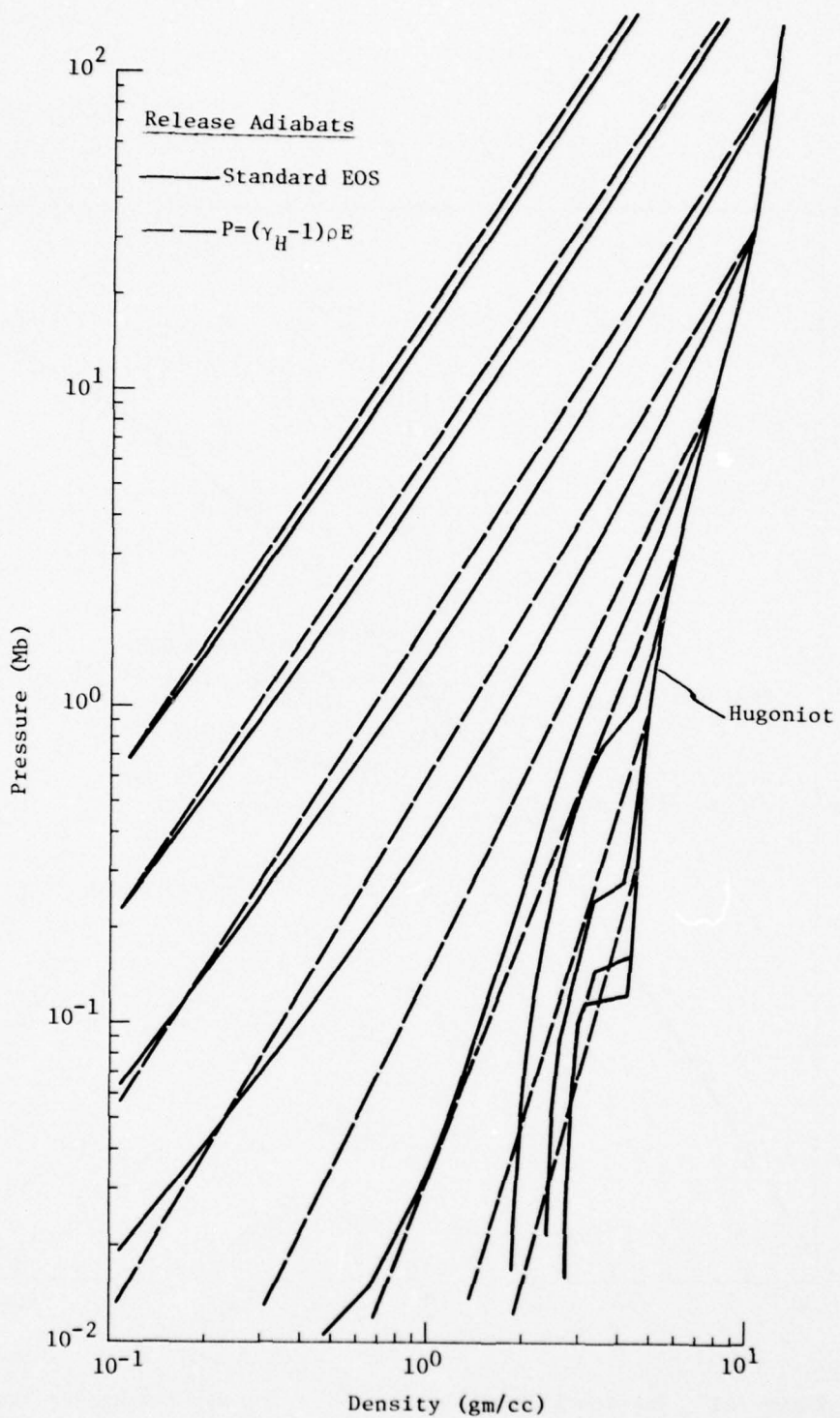


Figure 22. Hugoniot and Release Paths for Standard and Modified Pyatt Granite Equation of State.

antilog of the resulting number is determined. In Case B6, this procedure was replaced by simple linear interpolation, directly between the numbers in the table. The resulting TOA vs depth curve from Case B6 is virtually indistinguishable from the Baseline Case. This suggests either that the intervals between the values in the Pyatt EOS table are too fine (and that computer memory could be saved by reducing the table size), or that the costly process of using logs and antilogs could be replaced by simple direct interpolation between values in the tables.

4.2.3 Effects of EOS Model Under Other Conditions

To test the effects of the EOS model under other conditions, comparisons were made between the Pyatt and LASL models for cases in which the velocity and the internal energy level in the flyer plate were varied. (The LASL EOS was selected for these comparisons because of its use in the LASL 2-D calculations.)

The basic comparison of the Pyatt and LASL EOS models has been described in Section 4.2.1 above. In summary:

Case	EOS Model	Velocity	Internal Energy	Σ	Equivalent Kinetic Energy, E_{eff}
BL	Pyatt	50	~0	0	1.0
E6	LASL	50	~0	.080	1.19

Thus, use of the LASL model produces an effect on the calculated TOA which is equivalent to a 19% increase in flyer plate kinetic energy.

When the comparison is made at 40 cm/ μ sec, the following is obtained:

Case	EOS Model	Velocity	Internal Energy	Σ	Equivalent Kinetic Energy, E_{eff}
P2	Pyatt	40	~0	.212	.640
E6B	LASL	40	~0	-.101	.813

Under these conditions, the LASL EOS produces an effect equivalent to a 27% increase in flyer plate kinetic energy.

When a -40/70 cm/ μ sec ramp velocity is used, together with an internal energy level of 500 Mb-cc/gm in the flyer plate, these comparative results are obtained:

Case	EOS Model	Velocity	Internal Energy	Σ	Equivalent Kinetic Energy, E_{eff}
P16	Pyatt	-40/70	500	.015	1.032
E6A	LASL	-40/70	500	.092	1.225

Here, use of the LASL EOS is equivalent to increasing the flyer plate kinetic energy by 19%.

The above comparisons indicate that the effects of the EOS model are reasonably independent of the assumed velocity and internal energy conditions.

4.2.4 Preheating of Granite Block

In two cases, B4 and B5, it was assumed that the granite block is preheated by direct radiation from the nuclear source. For these runs, the internal energy density, IE_0 , at the front surface of the block was specified to be 0.2 and 20 Mb-cc/gm. Based on results of a preliminary S³ analyses, it was further

specified that the internal energy density in the block falls off with depth, D, within the block according to

$$IE_D = IE_0 \times 10^{-D/35}$$

The total initial internal energy added in the granite block due to preheat in Case B4 was approximately equal to the internal energy added to the flyer plate in Case P11. Similarly, the added internal energy in the block in Case B5 was about the same as that added to the plate in Case P12. (Cases P11 and P12 were discussed in Section 4.1.3.) It is therefore very interesting that the TOA vs depth curves for Cases B4 and P11, and for Cases B5 and P12, almost exactly coincide, as seen in Figure 14, on page 29. The Σ vs E_{tot} values for these cases also coincide (Figure 15, on page 30). Thus adding internal energy to the granite block has the same effect as adding the same internal energy to the flyer plates. In either case, adding a given amount of internal energy is the equivalent of adding about 3/4 of the same amount of kinetic energy. This again indicates that while the total amount of energy available has an important effect on the TOA vs depth in the granite block, the specific distribution of the energy has only a minor effect.

4.3 Numerical Parameters

4.3.1 Zone Size

All of the preceding cases used 1-D cells with initial thicknesses of 0.4 cm in the flyer plate and 0.4 cm near the face of the granite block. The thickness of cells in the block increased in 0.5% increments. These thicknesses were approximately the same as had been used in the 2-D analyses by S³, LASL, and SAI. To test the adequacy of this zoning, Case C1

was run in which all initial thicknesses were cut in half. The effect on TOA vs depth was quite small: cutting the zone size in half had an effect equivalent to increasing the kinetic energy by 2.2%. This suggest that the zoning in the 2-D studies was adequate.

4.3.2 Artificial Viscosity

Artificial viscosity is used in finite difference code solutions to provide stability across the discontinuity of the shock front. It has the effect of smearing the front over a few cells, and tends to reduce the peak pressure. In Case C2, the artificial viscosity parameter, Q, was changed from 4 (the value used throughout this study) to 1. The effect on TOA vs depth was negligible - equivalent to increasing the kinetic energy of the flyer plate by about 1%.

4.3.3 Energy Iteration

Since all of the codes used in the various HUSKY PUP studies were explicit in their formulation, there is a problem in calculating both pressure and energy at the same time. Many codes approach this problem by iterating the calculations of P and e until they converge. In CRALE-1, the final pressure and its derivative with respect to e are approximated by calculating a value based on the energy from the previous cycle and then adding the incremental change produced by the change in energy (-PdV). When this correction term was removed in Case C3, the effect on the TOA vs depth was negligible, suggesting that the potential error which could result from improper time-centering of the energy used in the pressure calculation is quite small. The iterative procedures used in some codes can be expensive, particularly if the EOS model is very complex; the results of Case C3 suggest these procedures could be simplified or even eliminated without serious loss of solution accuracy.

Figure 23 compares all of the TOA vs depth curves obtained when the above changes in the numerical parameters were made (Cases C1, C2, and C3). The effects are almost indescernible, indicating that these aspects of the numerics are not likely to have significantly influenced the 2-D calculations of TOA in the granite block.

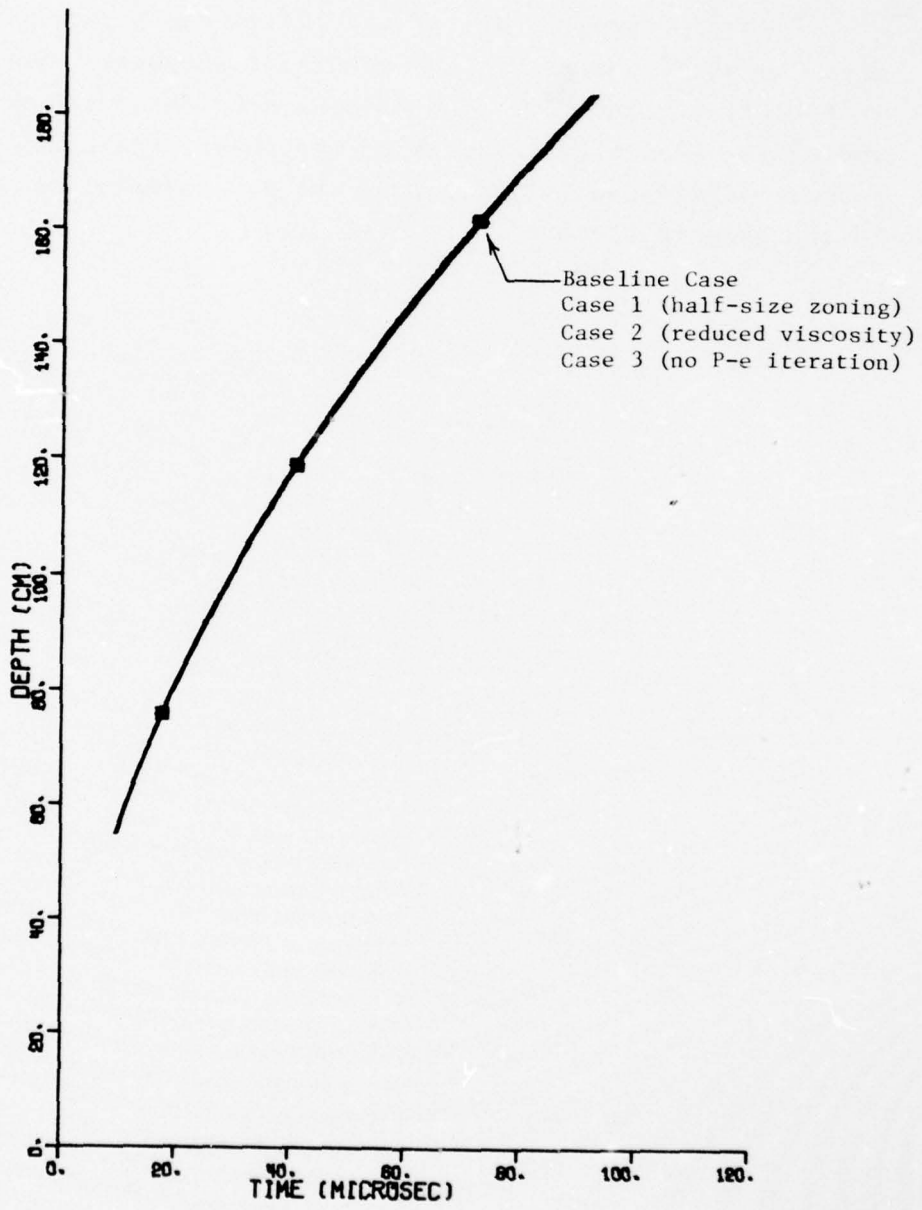


Figure 23. Variations in Time of Arrival Due to Changes in Numerical Techniques.

SECTION 5

DIFFERENCES IN EQUIVALENT KINETIC ENERGY BETWEEN EXPERIMENTAL DATA AND 2-D CALCULATIONS

It is of interest to determine the TOA sensitivity factor, Σ , and equivalent effective kinetic energy, E_{eff} , for the experimental TOA data and for the values obtained from the 2-D calculations. This is done by first calculating Σ by comparing these TOA vs depth curves with the curve from the Baseline Case (Figure 3 on page 10 and Figure 6 on page 15). Inserting these values for Σ in Figure 24, it is then possible to estimate the kinetic energy of the 1-D flyer plate which would produce essentially the same TOA vs depth curves as are seen in the experiment and in the results of the 2-D calculations. The absolute value of this equivalent kinetic energy is not of itself very significant, but the relative differences are a measure of how close the 2-D and 1-D calculations came to the measured data.

	TOA Sensitivity Factor, Σ	Equivalent Effective KE, E_{eff}	Difference of Value for Measured Data
Baseline 1-D Case	1.0	1.0	10%
HUSKY PUP Measured Data	.047	.91	-
LASL 2-D Calculation (pre-test)	-.135	.75	18%
S ³ 2-D Calculation (pre-test)	-.174	.70	23%
SAI 2-D Calculation (pre-test)	-.46	.33	64%

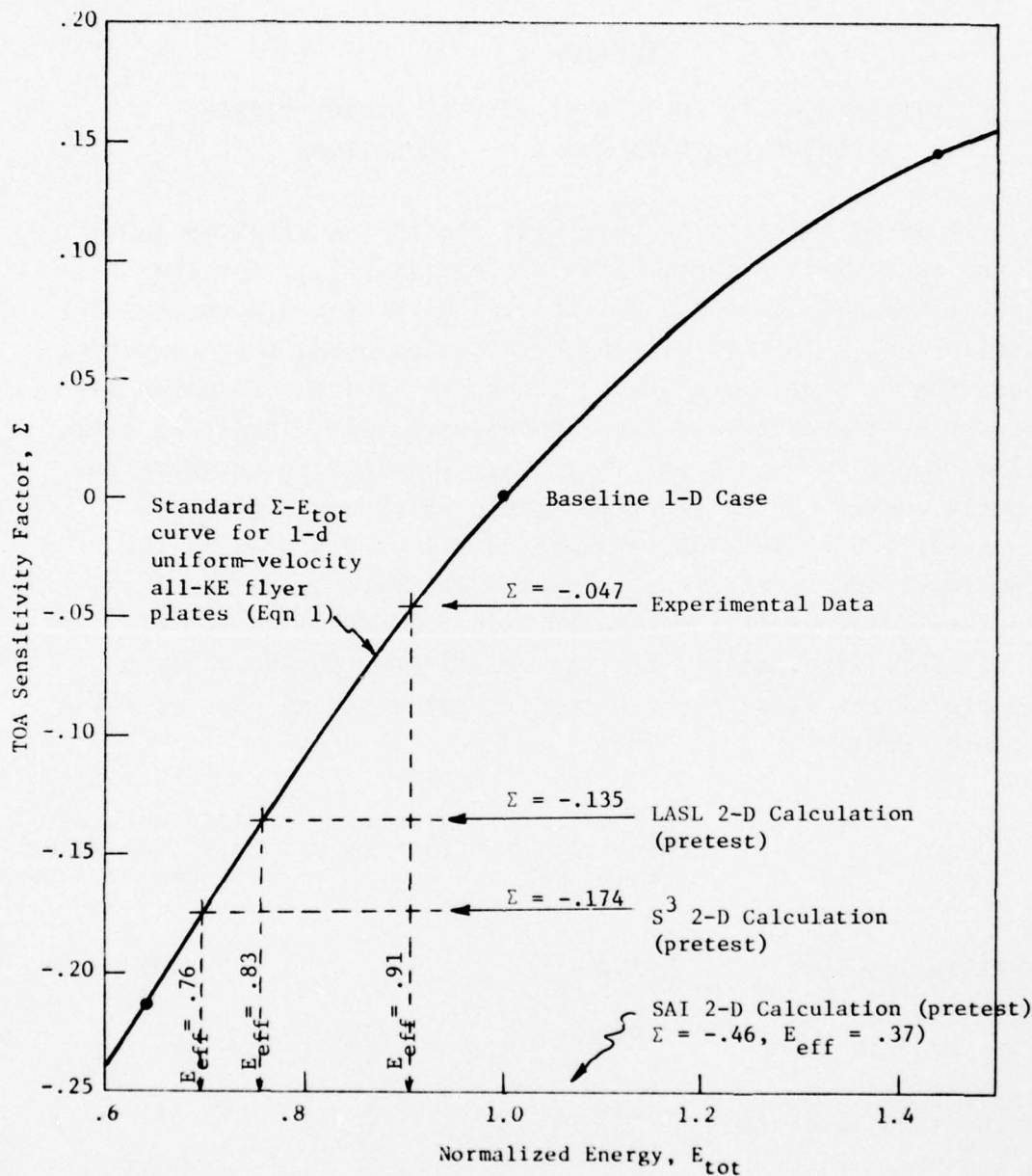


Figure 24. TOA Sensitivity Factor vs Normalized Energy. Values of Σ for the measured HUSKY PUP TOA data and for the 2-D Calculations have been determined in relation to the TOA curve for the 1-D Baseline Case. These Σ are then used to derive the KE of a 1-D flyer plate, E_{eff} , which would produce essentially the same TOA curves.

The LASL and S³ 2-D results are probably within the uncertainty limits of the HUSKY PUP source yield. This fact, plus the findings of the current study that calculations of TOA vs depth curves are insensitive to relatively large changes in input models and assumptions, indicates that further refinements of the LASL and S³ 2-D calculations are not necessary nor likely to be fruitful. We conclude that the technology demonstrated by these 2-D calculations is adequate to predict debris slap for cratering and ground motion analyses.

The major difference between the SAI 2-D results and the measurements and the results of the other 2-D calculations are not explainable, insofar as we can tell, by differences in the input assumptions. None of the variables or uncertainties which we considered in the current study appear likely to be responsible for the large discrepancy in the SAI results. This suggests the possibility of a calculational error of some type.

APPENDIX A

A SIMPLE INTERPRETATION OF THE HUSKY PUP TIME-OF-ARRIVAL DATA

Attempts were made in HUSKY PUP to measure pressures and velocities at various depths in the granite block. However, the only dependable data obtained were the times-of-arrival (TOA) of the first shock at the various gages. These data, shown in Figure A1, are quite consistent; a least squares fit of all the data in the form

$$D = at^b \quad (A1)$$

has an RMS error of less than 2%, independent of whether depth, D, is measured from the front surface of the block or the center of the source. The error drops to about 1% if only the Physics International (PI) ladder data are fit, and is smaller yet if either the earliest points are excluded, or an additive constant is used, i.e., $D = at^b + c$. The coefficients a and b fall into two classes, depending on whether the distance to the datum point is measured from the front surface of the block or the center of the device, Table A1.

A pressure vs range relationship can be derived by combining the fits to the TOA data with Hugoniot shock velocities, U_s , obtained from the EOS models. Curves of U_s vs P are shown in Figure A2 for two of the models. The shock velocities at any pressure above 1 Mb differ by less than 5% between the eight EOS models used in this study and can be approximated in the range .3 to 100 Mb by a power law, namely

$$U_s = dP^e \quad (A2)$$

where $d = .89$ and $e = .44$. This fit is included in Figure A2.

TABLE A1
ALTERNATIVE LEAST SQUARES FITS TO HUSKY PUP
TOA DATA AND INFERRED PRESSURE-DEPTH RELATIONSHIPS

$$(D = at^b + c) \quad (\text{TOA data})$$

$$(P = \alpha(D-c)^\beta) \quad (\text{inferred P-D relationship})$$

I. Where D is measured from center of device:

	a	b	c	α	β
Using all 27 data points:	36.18 ⁽¹⁾	.383 ⁽¹⁾	0 ⁽¹⁾	$2.61 \times 10^8^*$	-3.66*
or:	16.48	.517	35.31	6.5×10^4	-2.12
Using only PI ladder data:	36.99	.376	0		
or:	13.95	.553	40.03		
Using only last 7 ladder points:	34.86	.392	0		
or:	25.25	.446	16.97		

II. Where D is measured from front surface of granite block:

Using all 27 data points:	19.20 ⁽²⁾	.490 ⁽²⁾	0 ⁽²⁾	$2.3 \times 10^5^{**}$	-2.366**
Usingly only PI ladder data:	19.00	.494	0		
or:	15.25	.536	7.34		
Using only last 7 ladder points:	18.67	.499	0		
or:	18.66	.499	.004		

- (1) curve "Y" on Figure A1
- (2) curve "Z" on Figure A1
- * curve P_1 on Figure A3
- ** curve P_2 on Figure A3

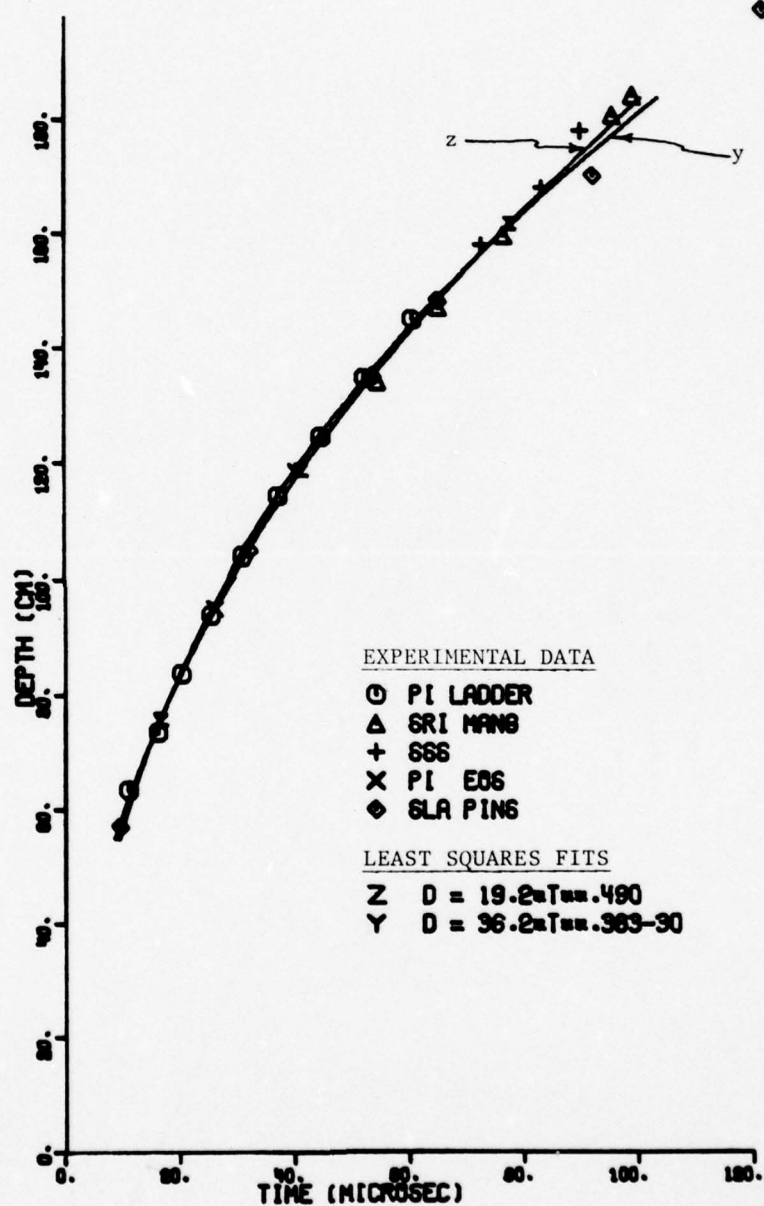


Figure A1. HUSKY PUP Time of Arrival Data and Two Least Squares Fits. (Depth Measured From the Front Surface of Granite Block.)

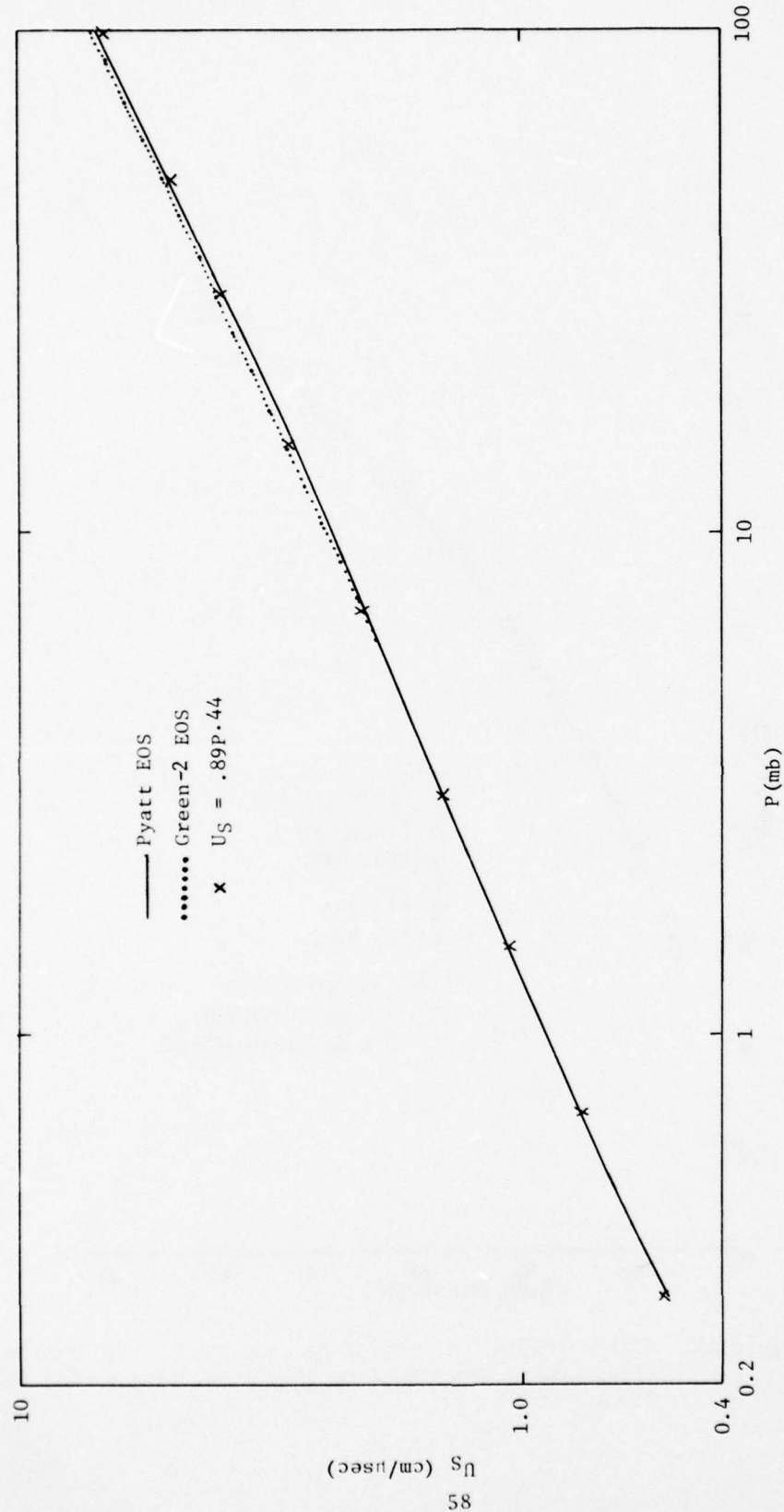


Figure A2. Shock Velocity vs Pressure in Granite.

Differentiating any of the curve fits listed in Table A1 provides a second equation for U_s which, together with the original fit, can be written as a function of position only,

$$U_s = ab \left[\frac{D-c}{a} \right]^{(b-1)/b} \quad (A3)$$

where a , b , c are the coefficients listed in Table A1. U_s can be eliminated in Equations A2 and A3 above to produce a pressure-distance relationship of the form

$$P = \alpha(D-c)^\beta \quad (A4)$$

where $\alpha = \left[(b/d)a^{1/b} \right]^{1/e}$ and $\beta = (\frac{b-1}{b})(\frac{1}{e})$

Two of the pressure vs depth curves derived from least squares fits of all the data points are presented in Figure A3. Since the curves represent two different fits to the same data, it is not surprising that they cross in the middle of the region of data. The small difference between shock velocities in the various EOS models, plus the rather small difference between the pressure vs depth fits in Figure A3 (less than 30% for all pressures above 0.7 Mb), suggest that the high pressure P-D relation is relatively insensitive to the EOS model or to the accuracy of individual data points.

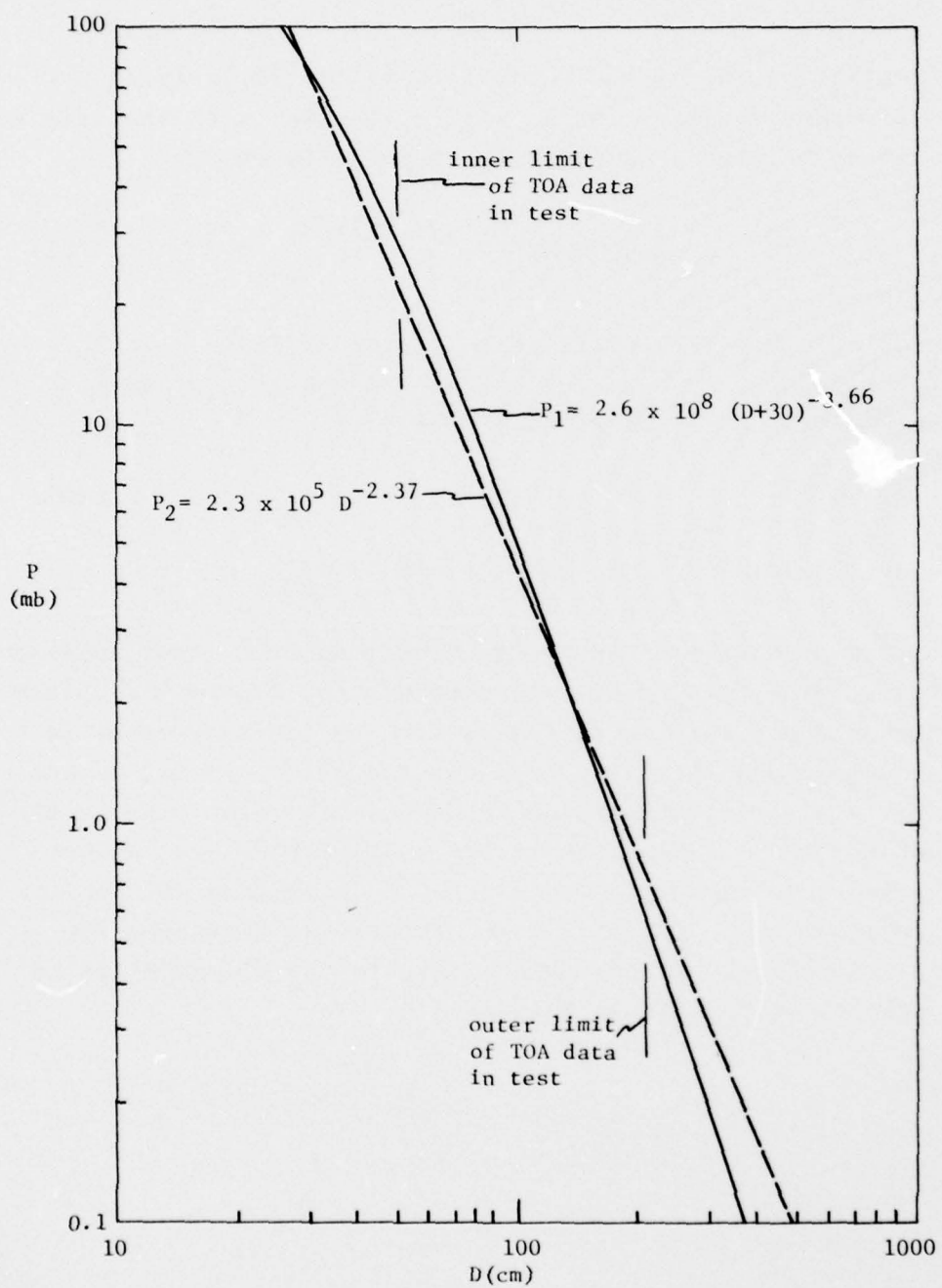


Figure A3. Peak Pressure as a Function of the Distance from the Front Surface of the Granite Block, Derived from the Theoretical Shock Velocity and Two Fits to the HUSKY PUP Time of Arrival Data.

APPENDIX B*

THE GRANITE EQUATION-OF-STATE FOR TEMPERATURES BETWEEN 0.5 EV and 1 KEV

B.1 Introduction

Eight models of the quartz (SiO_2) equation-of-state (EOS) have been studied to estimate the potential error in prediction calculations of the HUSKY PUP granite block experiments caused by uncertainties in high energy material properties. Of specific concern was the material behavior in the temperature range between 0.5 eV and 1.0 keV. Radiation effects dominate the calculation above 1 keV (10^{15} ergs/gm), while the various experiments of interest in HUSKY PUP occur at temperatures above 0.5 eV. The temperature range of interest is well above that of most previous experiments, but it is too low to expect simple Thomas-Fermi or Saha models to be entirely valid. Of the eight specific models investigated (Table B1 and References 5 through 12), one was based on the Saha equation (5); the other seven used the Thomas Fermi theory (12) with various corrections and/or approximations. Comparisons of the Hugoniots and release adiabats for all of the models are presented in Section B.2, while specific characteristics of each model are discussed briefly in Section B.3.

* This appendix was originally a memo written while one of the authors (Schuster) was at R & D Associates and represents work sponsored there by DNA.

Table B1. SiO_2^* EOS MODELS STUDIED

AUTHOR	THEORY	TYPE	REFERENCE
1. PYATT (S ³)	SAHA	TABLE LOOKUP	5
2. BARYNE (LASL)	THOMAS-FERMI	"	6
3. GREEN 1 (RDA)	"	"	7
4. " 2 (RDA)	" a	"	7
5. " 3 (RDA)	" b	"	7
6. KALITKIN (USSR/LLL)	" c	"	8,9
7. SCHUSTER (RDA)	"	ANALYTIC FIT	10
8. TILLOTSON (GA)	"	"	11

$$* \rho_0 = 2.65 \text{ gm/cm}^3$$

^aIncludes nuclear correction assuming nuclei behave as a perfect gas.

^bIncludes nuclear correction assuming nuclei behave as harmonic oscillators.

^cIncludes electron exchange and correlation corrections.

B.2 Comparisons of Various Models

Since dissipation from energy densities between 10^{11} and 10^{15} ergs/gm always involve shock processes, the principal Hugoniot is a useful curve for comparing various models. The jump conditions at a shock front, combined with each EOS model, are sufficient to determine the locus of points attainable in a strong shock, i.e., the principal Hugoniot. The jump conditions are:

$$\rho_0 S = \rho(S-U) \quad (\text{conservation of mass}) \quad (B1)$$

$$E = U^2/2 \quad (\text{conservation of energy}) \quad (B2)$$

$$P = \rho_0 S U \quad (\text{conservation of momentum}) \quad (B3)$$

where ρ_0 and ρ are the pre- and post-shock densities of the material, U and S are the material and shock speeds, E is the energy density, and P is the shock pressure. Strictly speaking, P , E , and U represent changes in those quantities, but along the principal Hugoniot the initial pressure, energy and material velocity of the rock are small and can be ignored. Since the above three equations contain five unknowns, adding a fourth equation, namely the EOS model, allows one to solve for any four of the unknowns as a function of the fifth. The resulting Hugoniots, represented as P vs ρ , are shown in Figure B1.

All of the curves coalesce near 1 mbar since they were forced to match the low pressure (<5 Mb) experimental data.

At higher pressures the Kalitkin, Pyatt, and Green 3 models are considerably softer, i.e., more compressible, than the other five models which remain in a tight band. At very high pressures all of the models approach an effective gamma [$\gamma_e = (P + \rho E)/\rho E$] of 5/3 except for the Tillotson model which converges to a value of 3/2. While there appear to be rather striking differences between the various Hugoniots, the energy deposited in the

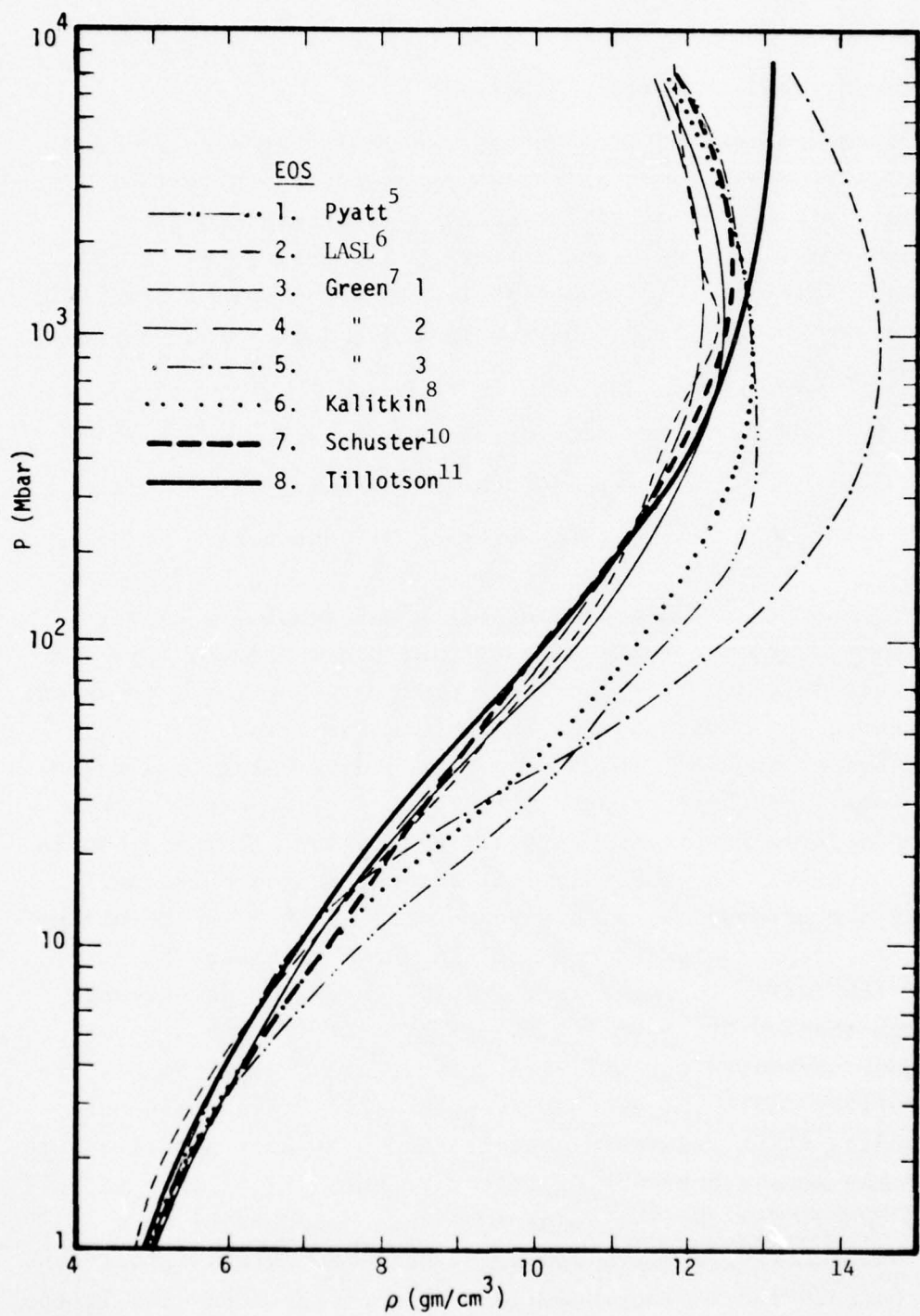


Figure B1. Principal Hugoniots Calculated from the Eight Models for Quartz

material at any given pressure does not vary greatly even between the extremes of the curves. Expressing the Hugoniot energy as a function of pressure and effective gamma, namely

$$E = \frac{P}{\rho_0(\gamma_e + 1)} \quad (B4)$$

it follows that at any specific value of the pressure, the ratio of deposited energies between any two models is simply

$$R(E) = \frac{\gamma_1 + 1}{\gamma_2 + 1} \quad (B5)$$

Although in theory, γ_e can vary between 1 and ∞ , for pressures above 5 mbars the effective gamma along the Hugoniot for any of the models studied was never less than 1.44 or greater than 2.6*. In addition, at any pressure, the effective gammas for the extreme Hugoniots never differ by more than 40%, so that the maximum variation in energy is less than 12%, Figure B2. The ratio of shock velocities is even less sensitive to differences in the Hugoniots, varying as $\sqrt{R(E)}$. Thus, the differences between the models shown in Figure B1 are probably not important to a calculation of the overall material response, particularly if one considers that the Hugoniot is only the loci of states, only one of which is reached by any specific zone of material in a calculation. Of much greater potential significance are any systematic differences in release adiabats from the various Hugoniots. While the energy deposited by a given magnitude shock does not vary greatly between the models, if

* Below 5 mbar the material is a solid and cannot be realistically represented by a γ -law equation.

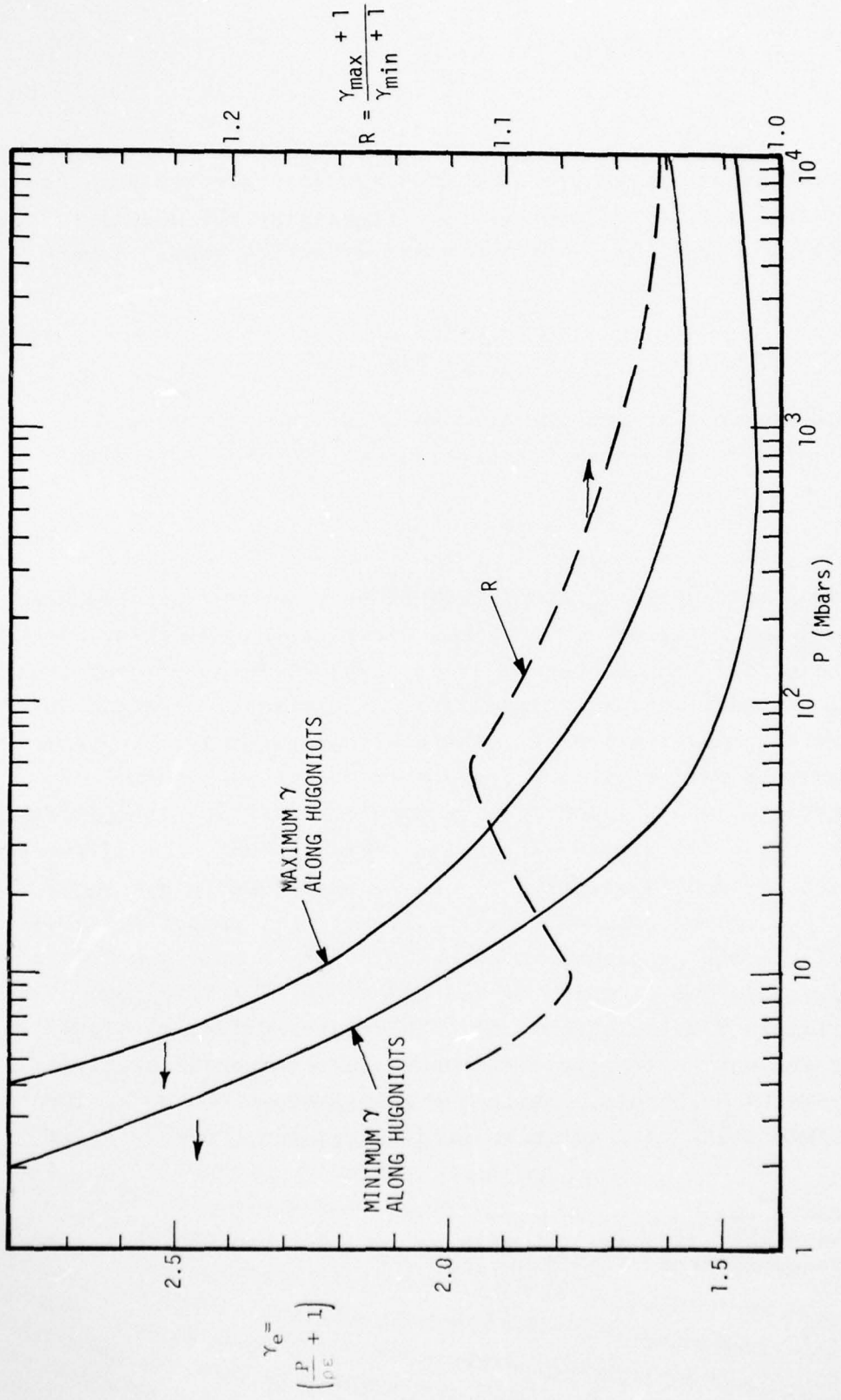


Figure B2. Bounds of Effective Gamma Along Calculated Hugoniots and the Maximum Ratio of Energy Deposited as Functions of Shock Pressure

the fraction of the energy recovered during the adiabatic expansion was to differ, the effect could be dramatic. Such does not appear to be the case, as release adiabats from 10, 100, and 1000 Mbars (Figure B3), appear to cluster tightly in P- ρ space. Even when plotted on the energy-volume plane (Figure B4), the differences for release from 100 and 1000 Mbar are not great. The energies lost in waste heat after expansion to 100 cm^3/gm differ by a factor of 4 between the extremes of the models. However, these energies are an order of magnitude less than the initial energy deposited, so the *energy recovered* only varies between 91 and 97.5%. Furthermore, the spread between the presumably more accurate six table look-up models is only 2% (95.5-97.5%). The larger spread for the 10 Mbar unloading is due to the differences between the models' treatment of the solid phase of SiO_2 and while important for low stress attenuation, was not a subject of this review.

An additional set of unloading paths from the point $\rho = \rho_0 (2.65 \text{ g/cm}^3)$ and $E = 10^{15} \text{ ergs/cm}$, shown in Figure B4, simulates release after the instantaneous deposition of energy into cold material. While not an exact representation of radiation deposition, this state is typical of the initial conditions frequently used in calculations of nuclear explosions. The six table look-up models return between 88 and 92 percent of the initial energy during expansion to 100 cm^3/gm , while the two analytic fits (Tillotson's and Schuster's), recover 94 and 97.5%, respectively. If one assumes that the energy recovered and available to do continuing work is the most significant driving mechanism of the ground motions, the differences exhibited in Figures B1 through B4 do not appear significantly large.

Two further questions remain: First, do the models presented here really cover the complete range of possible material behavior, i.e., could the real material load and/or unload along paths outside the limits of our models? Second, how critical is the time scale over which the material unloads?

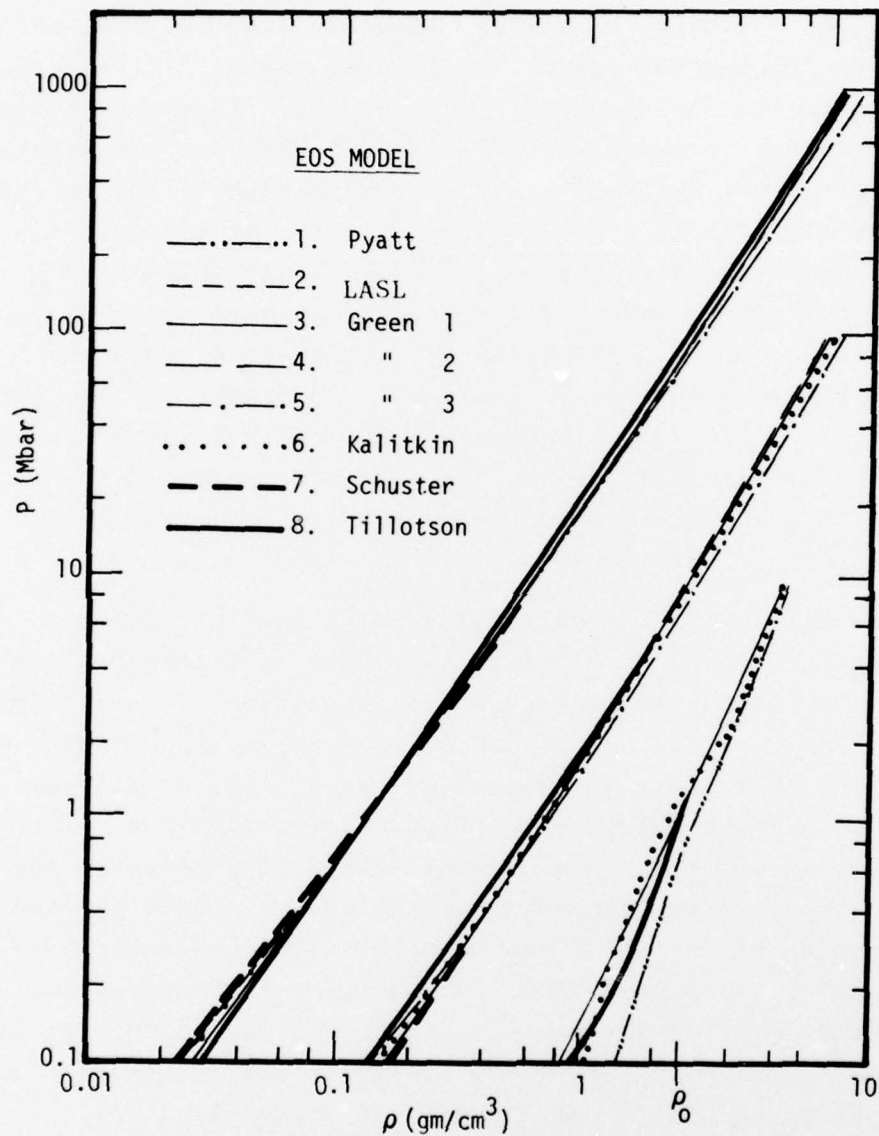


Figure B3. Release Adiabats from ~10, 100, and 1000 Mbar Hugoniot Pressures for Quartz. (Several curves are deleted where they coalesce with the others)

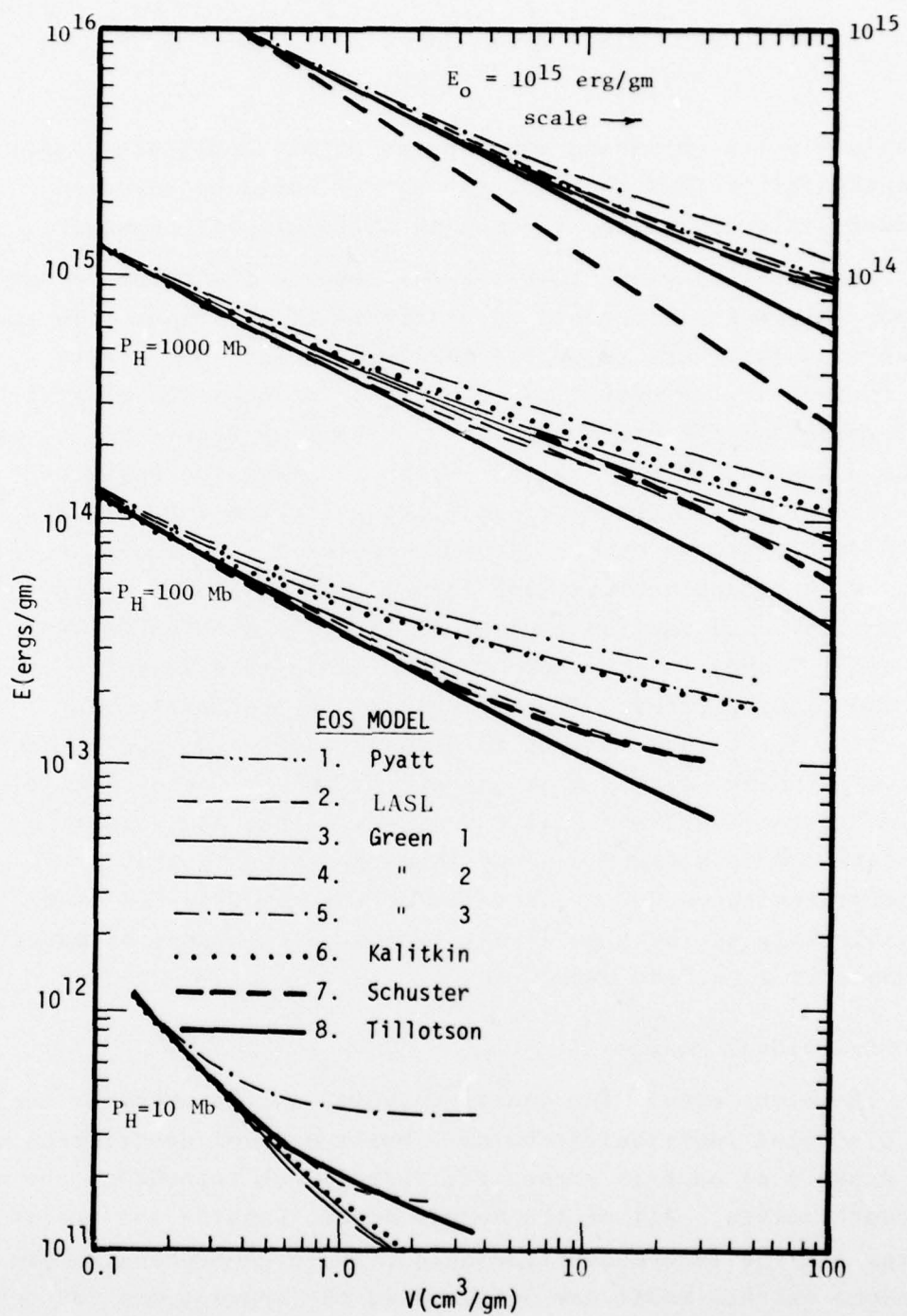


Figure B4. Release Adiabats from ~ 10 , 100 and 1000 Mbar. Hugoniot Pressures and from $\rho = \rho_0$, $E = 10^{15}$ ergs/gm for Quartz
(Several curves are deleted where they coalesce with the others)

Clearly, if the unloading wave speeds of one model are significantly faster than another, the energy would be released quicker and could change the motion at lower peak pressures.

The question of whether one has covered the complete set of possible material models is difficult if not impossible to answer; however, the issue has been addressed. One simple way to look at the models is to express the equation-of-state in terms of an effective gamma, γ_e . Thus, in Figure B5, γ_e vs ρ for unloading from $\rho = \rho_0$, $E = 10^{15}$ and from the Hugoniot pressure of about 1000 Mbar, is plotted for the two extremes of the table lookup models (Green's tables of the Thomas-Fermi model with the perfect gas and harmonic oscillator nuclear corrections) and the two analytical fits. γ_e varies between 1.2 and 1.7 over the pressure range 0.02 to 1000 Mbar for the release paths plotted. While gamma can theoretically vary from 1 to ∞ , it is difficult to imagine a material whose gamma is consistently below 1.3 or above 1.7 for the energy densities of interest. Thus, the static analysis of the SiO_2 equation-of-state models presented above strongly suggests that for temperatures above 0.5 eV, details of the specific EOS used probably will not be significant in the calculations of material response to a nuclear explosion.

B.3 Individual Models

The eight models for quartz compared in the previous section are discussed individually below. While a brief description of the aspects of each is presented, this is not intended to be an in-depth review. All of the models assume density and specific energy are the independent variables. More comprehensive discussions of each model may be found in the appropriate references listed in Table B1.

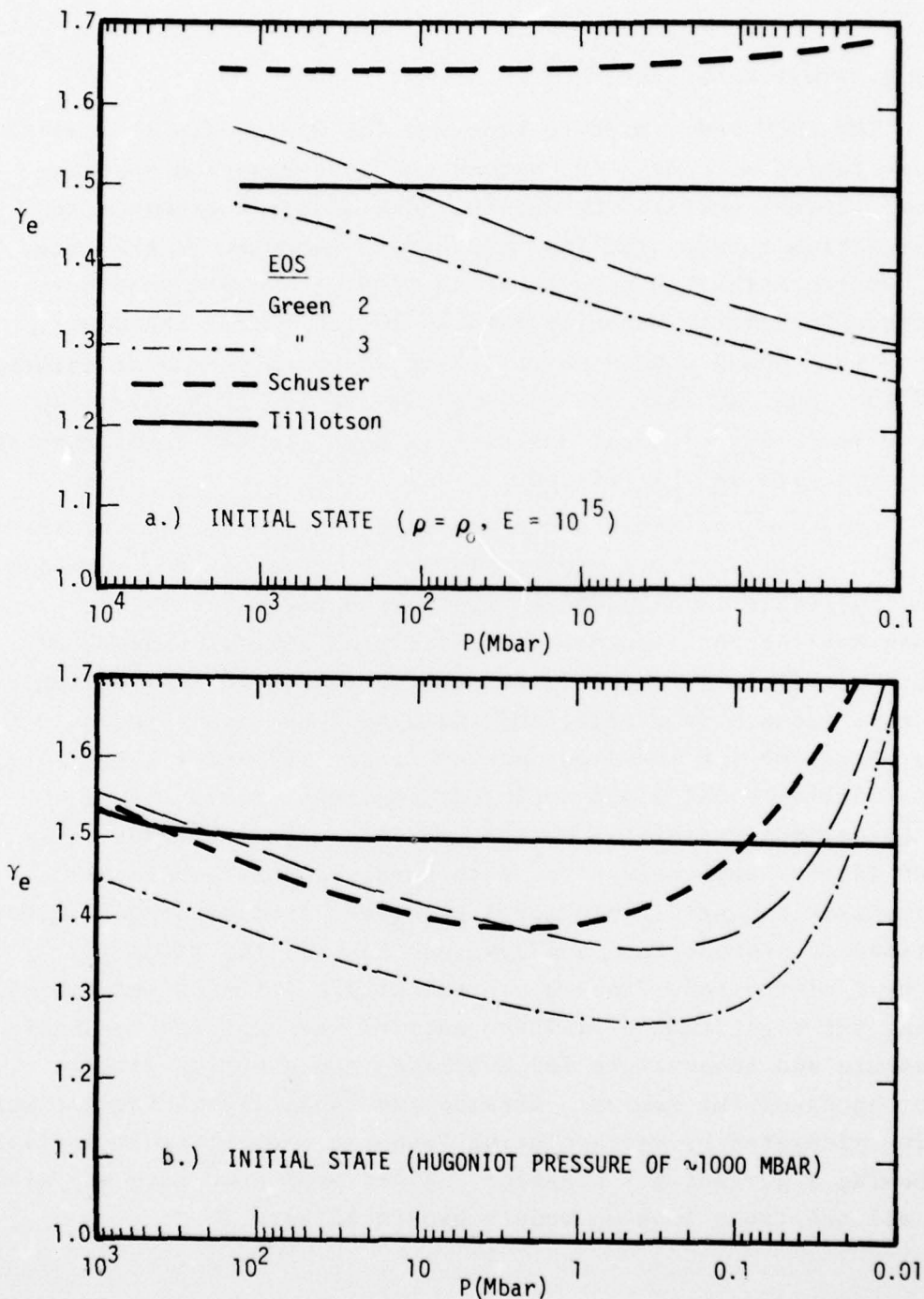


Figure B5. Effective Gamma, γ_e , vs Pressure During Release from Two Initial States

B.3.1 Pyatt Model (S^3)

The CAPO code, used to generate the basic data from which these tables were derived, solves the Saha equation assuming local thermal equilibrium and includes electron exchange and correlation terms. The low temperature behavior is presented by a Birch-Murnaghan type equation with parameters chosen to match experimental Hugoniot data up to 120 kbar. The quartz-stishovite phase change which occurs at shock pressures between 120 kbar and 350 kbar was included at the 120 kbar level, so the calculated principal Hugoniot is consistently lower than the measured data in this region.

Pressure and temperature are each represented by a coarse and fine table in this model. This two table scheme, in which the fine table is embedded in the coarse, was necessary to represent the phase change without a prohibitively large computer storage requirement. The coarse tables were dimensioned 23 x 38 (density x energy) and included densities between 10^{-3} and 25 gm/cm^3 and energies between 1.58×10^8 and $4 \times 10^{15} \text{ ergs/gm}$. The fine table (53 x 53) included densities between 1 and 10 gm/cm^3 and energies from 10^8 and 10^{12} ergs/gm . Thus only 7400 entries were needed for both pressure and temperature. (A comparable single table model generated earlier needed 23,000 entries to provide the same coverage and was too large for several of the codes to use conveniently.) A linear interpolation using the logarithms of all the entries was employed to obtain pressure and temperature for densities and energies within the bounds of the tables. Outside the table limits the pressures were calculated by extrapolating from the nearest table entries assuming a perfect gas behavior. (This same procedure was used in all the table look-up models presented here.)

B.3.2 Barnes Model (LASL)

The standard LASL EOS is derived from the Thomas-Fermi (T-F) formulation for an electron gas. The solid behavior, high-temperature nuclear motion and electron exchange and correlations forces are included. Pressure and temperature are found by a two-step process in this model. First, the pressure, P_0 , and energy, E_0 , at the desired density, are calculated for the zero degree isotherm by interpolating in two 33 entry tables. The thermal contribution to pressure and the temperature are then calculated from 33×16 tables (density x energy) using the density and thermal energy ($E - E_0$). The tables include densities and energies from 0.02 to 14.4 gm/cm^3 and 0 to $2.64 \times 10^{14} \text{ ergs/gm}$ respectively. Since the tables for thermal energy start from zero, a linear interpolation of the actual values rather than their logs was necessary.

B.3.3 Green 1 Model (RDA)

J. Green (RDA) derived data for this model by fixing the temperature and the electron-free energy, and using Latter's T-F results to obtain the resulting pressure, energy, partial volumes, and entropy contributed by the electrons from both the silicon and the oxygen atoms. Since the electrons of both atoms are in thermodynamic equilibrium if they share a common temperature and electron-free energy, the electronic pressures are the same at the atomic interfaces. The pressure of the mixture, therefore, is the pressure at the edge of either atom.

The original density, pressure, and energy output was converted into 30×27 tables ($\rho \times E$) of pressure and temperature by an auxilliary routine. In addition, since the T-F model used is only valid for a hot electron gas, at energy densities less than $3 \times 10^{11} \text{ ergs/gm}$ the pressure was calculated using the

low pressure portion of the Schuster analytic fit. A simple weighting function was used to go smoothly between the fit and the tables for energies between 0.3 and 3.0×10^{12} ergs/gm, i.e.,

$$P = f P_{\text{fit}} + (1-f) P_{\text{table}} \quad (\text{B6})$$

where

$$f = \frac{E - 0.5 \times 10^{12}}{3 \times 10^{12}} \quad (\text{B7})$$

The logarithmic interpolation routine used for the Pyatt tables was also used for all the Green & Kalitkin tables.

B.3.4 Green 2 Model (RDA)

The second Green model differs from the one above in that the effects of nuclear motion are included by assuming the nuclei behave as a perfect gas with three degrees of freedom. This results in an increase in both pressure and energy at a given temperature and shifts the Hugoniot slightly to the left (less compressible) in $P-\rho$ space (Figure B1).

B.3.5 Green-3 Model (RDA)

Again, the original Green model was modified by a nuclear motion contribution, this time assuming the nuclei are bound by a harmonic well. The nuclei, therefore, contribute nothing to the pressure but add 3 kt per nucleus to the energy, producing a significant softening of the Hugoniot, shifting it to the right in Figure B1.

The two models of nuclear motions are exceedingly useful since they should represent upper and lower limits of this effect on the pressure. As shown in Figure B1, above 50 Mbar the Hugoniots produced by the Green-2 and -3 models do indeed bound the other curves.

B.3.6 Kalitkin Model

Corrections to the basic T-F description for the electron quantum and exchange forces at 0°K were derived by Kalitkin. These changes were extended at LLL and incorporated in a code which generates tables of pressure, energy, and correction terms, ΔP and ΔE as functions of density, temperature and atomic number. By assuming an average atomic weight of 10.662, appropriate high energy tables were generated for quartz. Again the Schuster fit was used at low energies.

The average atom approximation is cruder than equating temperature and free energy as in the Green models. However, setting ΔP and ΔE to zero produced an EOS which overlays that of Green-1, so the two methods appear equivalent for quartz. The Kalitkin model, therefore, can be compared with the other T-F models to estimate the effects of the electron correction terms.

B.3.7 Schuster Model (RDA)

In an attempt to get a simple analytic EOS for quartz, an expression was found to approximate the effective gamma calculated from the Green-1 model. The resulting expression

$$(\gamma - 1) = (0.35 \log \frac{E}{\rho} - 0.464)^2 + 0.4 + 0.12 \log \rho \quad (B8)$$

provides a gas pressure (assuming a perfect gas) which is then added to the solid phase contribution. The resulting Hugoniot and associated release adiabats, Figures B1 and B3, are in reasonable agreement with those of Green-1. The unloading from normal density and $E = 10^{15}$ ergs/gm differ markedly, however, suggesting a better fit should be found if this model is to be used in future calculations.

B.3.8 Tillotson (GA) Model

An analytical fit, first derived by J. Tillotson for hypervelocity impact studies of metals has been used extensively in calculations of motions in rocks. The fit has two parts, one which models the solid behavior (using a polynomial) and the second which represents the gaseous state. The gas term has a perfect gas form $P = (\gamma-1)\rho E$, in which the gamma is allowed to vary thusly:

$$(\gamma-1) = a + \frac{b}{\frac{E}{E_0}^2 + 1} \quad (B9)$$

At high energies this equation reduces to $\gamma-1 = a$, where a has historically been assumed to be 0.5. As seen in Figure B1, the resulting Hugoniot is consistent with several of the other models up to 1000 Mbar. Above this pressure the effective gamma of the other models begin to increase asymptotically to 5/3 while the Tillotson value remains at 1.5

REFERENCES

1. J. Lille, Los Alamos Science Laboratory, (private communication).
2. E. Bailey, "Calculation and Analysis of the HUSKY PUP Add-on Coupling Experiment", Systems, Science, and Software, DNA 4081F, August 1976.
3. R. Schlaug, Science Applications, Inc., (private communication).
4. J. Whitener, R & D Associates, (private communication).
5. K. D. Pyatt, Systems, Science, and Software, (private communication).
6. J. Barnes, Los Alamos Science Laboratory, (private communication), also see S. L. Thompson and H. S. Larson, "Improvements in the Chart D Radiation Hydrodynamic Code III: Revised Analytic Equation of State", Sandia Laboratories, SC-RR-71-0714, March 1972.
7. J. M. Green, "Preliminary Results of Thomas-Fermi Equation-of-State Study of SiO₂", R & D Associates, RDA interoffice memorandum, February 17, 1975.
8. N. N. Kalitkin, "The Thomas-Fermi Model of the Atom with Quantum and Exchange Corrections", JETP, Vol. II, No. 5, November 1960.
9. T. J. Ahrens, California Institute of Technology, (private communication).
10. S. H. Schuster and J. Isenberg, "Equation-of-State for Geologic Materials", Applied Theory, Inc., DNA 2925Z, September 1972.
11. J. Tillotson, "Metallic Equation-of-State for Hypervelocity Impact", General Atomic Division, General Dynamics, GA-3216, 1967.
12. R. Latter, Phy. Rev., Vol. 99, p. 1854, 1955, and J. Chem. Phys., Vol 23, p. 280, 1956.

DISTRIBUTION LIST

DEPARTMENT OF DEFENSE

Assistant to the Secretary of Defense
 Atomic Energy
 ATTN: Honorable Donald R. Cotter

Director
 Defense Advanced Rsch. Proj. Agency
 ATTN: Tech. Lib.
 ATTN: NMRO
 ATTN: PMO
 ATTN: STO

Director
 Defense Civil Preparedness Agency
 Assistant Director for Research
 ATTN: Admin. Officer

Defense Communications Agency
 WWMCCS System Engineering Org.
 ATTN: Thomas Neighbors

Defense Documentation Center
 Cameron Station
 12 cy ATTN: TC

Director
 Defense Intelligence Agency
 ATTN: DI-7E
 ATTN: DB-4C, Edward O'Farrell
 ATTN: DT-1C

Director
 Defense Nuclear Agency
 2 cy ATTN: SPSS
 ATTN: TISI Archives
 3 cy ATTN: TITL, Tech. Lib.
 ATTN: DDST

Commander, Field Command
 Defense Nuclear Agency
 ATTN: FCPR

Director
 Interservice Nuclear Weapons School
 ATTN: Document Control

Director
 Joint Strat. Tgt. Planning Staff, JCS
 ATTN: STINFO Library

Chief
 Livermore Division, Field Command, DNA
 Lawrence Livermore Laboratory
 ATTN: FCPRL

Under Secretary of Def. for Rsch. & Engrg.
 ATTN: S&S (OS)

DEPARTMENT OF THE ARMY

Director
 BMD Advanced Tech. Ctr.
 Huntsville Office
 ATTN: CRDABH-S
 ATTN: 1CRDABH-X

DEPARTMENT OF THE ARMY (Continued)

Dep. Chief of Staff for Rsch. Dev. & Acq.
 ATTN: Tech. Lib.

Chief of Engineers
 ATTN: DAEN-MCE-D
 ATTN: DAEN-RDM

Dep. Chief of Staff for Ops. & Plans
 ATTN: Tech. Lib.

Commander
 Harry Diamond Laboratories
 ATTN: DRXDO-TI, Tech. Lib.
 ATTN: DELHD-NP

Commander
 Redstone Scientific Information Ctr.
 U.S. Army Missile Command
 ATTN: Chief, Documents

Director
 U.S. Army Ballistic Research Labs.
 ATTN: DRXBR-X, Julius J. Meszaros
 ATTN: Tech. Lib., Edward Baicy
 ATTN: DRDAR-BLE, W. Taylor
 ATTN: DRDAR-BLE, J. H. Keefer

Commander
 U.S. Army Engineer Center
 ATTN: ATSEN-SY-L

Division Engineer
 U.S. Army Engineer Div., Huntsville
 ATTN: HNDED-SR

Division Engineer
 U.S. Army Engineer Div., Ohio River
 ATTN: Tech. Lib.

Director
 U.S. Army Engr. Waterways Exper. Sta.
 ATTN: Tech. Lib.
 ATTN: Guy Jackson
 ATTN: John N. Strange
 ATTN: Leo Ingram
 ATTN: William Flathau

Commander
 U.S. Army Mat. & Mechanics Rsch. Ctr.
 ATTN: Tech. Lib.

Commander
 U.S. Army Materiel Dev. & Readiness Cmd.
 ATTN: Tech. Lib.

Commander
 U.S. Army Nuclear Agency
 ATTN: Tech. Lib.

DEPARTMENT OF THE NAVY

Chief of Naval Material
 ATTN: MAT 0323

DEPARTMENT OF THE NAVY (Continued)

Chief of Naval Operations
ATTN: Op-981
ATTN: Op-03EG

Chief of Naval Research
ATTN: Tech. Lib.
ATTN: Nicholas Perrone
ATTN: Code 464, Jacob L. Warner
ATTN: Code 464, Thomas P. Quinn

Officer-in-Charge
Civil Engineering Laboratory
Naval Construction Battalion Center
ATTN: Stan Takashashi
ATTN: Tech. Lib.

Commander
David W. Taylor Naval Ship R&D Center
ATTN: Code L42-3, Library

Commander
Naval Electronic Systems Command
Naval Electronic Systems Cmd. Hqs.
ATTN: PME 117-21A

Commander
Naval Facilities Engineering Command
ATTN: Code 03A
ATTN: Code 04B
ATTN: Tech. Lib.

Superintendent (Code 1424)
Naval Postgraduate School
ATTN: Code 2124, Tech. Rpts. Librarian

Director
Naval Research Laboratory
ATTN: Code 2600, Tech. Lib.

Commander
Naval Sea Systems Command
ATTN: ORD-91313, Lib.

Commander
Naval Ship Engineering Center
ATTN: Tech. Lib.

Commander
Naval Ship Rsch. & Development Ctr.
Underwater Explosive Research Div.
ATTN: Tech. Lib.

Officer-in-Charge
Naval Surface Weapons Center
ATTN: Code WA501, Navy Nuc. Prgms. Off.

Commander
Naval Surface Weapons Center
Dahlgren Laboratory
ATTN: Tech. Lib.

President
Naval War College
ATTN: Tech. Library

Commanding Officer
Naval Weapons Evaluation Facility
ATTN: Tech. Lib.

DEPARTMENT OF THE NAVY (Continued)

Director
Strategic Systems Project Office
ATTN: NSP-43, Tech. Lib.

DEPARTMENT OF THE AIR FORCE

AF Geophysics Laboratory, AFSC
ATTN: SUOL, Rsch. Lib.

AF Institute of Technology, AU
ATTN: Library AFIT, Bldg. 640, Area B

AF Weapons Laboratory, AFSC
ATTN: SUL
ATTN: DES-S, M. A. Plamondon
ATTN: DYT
ATTN: DES-C, Robert Henny

Headquarters
Air Force Systems Command
ATTN: DLCAW

Commander
Foreign Technology Division, AFSC
ATTN: NICD Library

Hq. USAF/IN
ATTN: INATA

Hq. USAF/PR
ATTN: PRE

Hq. USAF/RD
ATTN: RDQSM

Commander
Rome Air Development Center, AFSC
ATTN: EMTLD, Doc. Lib.

SAMSO/MN
ATTN: MMH

Commander in Chief
Strategic Air Command
ATTN: NRI-STINFO, Lib.

DEPARTMENT OF ENERGY

Department of Energy
Albuquerque Operations Office
ATTN: Doc. Con. for Tech. Lib.

Department of Energy
Division of Headquarters Services
ATTN: Doc. Con. for Class. Tech. Lib.

Department of Energy
Nevada Operations Office
ATTN: Doc. Con. for Tech. Lib.

University of California
Lawrence Livermore Laboratory
ATTN: Tech. Info., Dept. L-3

Los Alamos Scientific Laboratory
ATTN: Doc. Con. for R. J. Bridwell
ATTN: Doc. Con. for Reports Lib.
ATTN: Doc. Con. for G. R. Spillman

DEPARTMENT OF ENERGY (Continued)

Sandia Laboratories
Livermore Laboratory
ATTN: Doc. Con. for Tech. Lib.

Sandia Laboratories
ATTN: Doc. Con. for 3141, Sandia Rpt. Coll.

Union Carbide Corporation
Holifield National Laboratory
ATTN: Doc. Con. for Tech. Lib.
ATTN: Civil Def. Res. Proj.

OTHER GOVERNMENT AGENCY

Department of the Interior
Bureau of Mines
ATTN: Tech. Lib.

DEPARTMENT OF DEFENSE CONTRACTORS

Aerospace Corporation
ATTN: Tech. Info. Services

Agbabian Associates
ATTN: M. Agbabian

Applied Theory, Inc.
2 cy ATTN: John G. Trulio

Avco Research & Systems Group
ATTN: Research Lib., A830, Rm. 7201

Battelle Memorial Institute
ATTN: Tech. Lib.

The BDM Corporation
ATTN: Tech. Lib.

The Boeing Company
ATTN: R. M. Schmidt
ATTN: Aerospace Lib.

California Research & Technology Inc.
ATTN: Ken Kreyenhagen
ATTN: Sheldon Shuster
ATTN: Tech. Lib.

Calspan Corporation
ATTN: Tech. Lib.

Civil/Nuclear Systems Corp.
ATTN: Robert Crawford

University of Dayton
Industrial Security Super KL-505
ATTN: Hallock F. Swift

University of Denver
Colorado Seminary
Denver Research Institute
ATTN: Sec. Officer for J. Wisotski

EG&G, Inc.
Albuquerque Division
ATTN: Tech. Lib.

Gard, Inc.
ATTN: G. L. Neidhardt

DEPARTMENT OF DEFENSE CONTRACTORS (Continued)

General Electric Company
TEMPO-Center for Advanced Studies
ATTN: DASIAC

IIT Research Institute
ATTN: Tech. Lib.

Institute for Defense Analyses
ATTN: IDA Librarian, Ruth S. Smith

Kaman AviDyne
Division of Kaman Sciences Corp.
ATTN: Tech. Lib.
ATTN: E. S. Criscione

Kaman Sciences Corporation
ATTN: Library

Lockheed Missiles & Space Co., Inc.
ATTN: Tech. Lib.

Lockheed Missiles & Space Co., Inc.
ATTN: Tech. Info. Ctr., D/Coll.
ATTN: Tom Geers, D/52-33, Bldg. 205

McDonnell Douglas Corporation
ATTN: Robert W. Halprin

Merritt CASES, Inc.
ATTN: J. L. Merritt
ATTN: Tech. Lib.

Nathan M. Newmark
Consulting Engineering Services
ATTN: Nathan M. Newmark

Physics International Company
ATTN: Doc. Con. for Dennis Orphal
ATTN: Doc. Con. for Fred M. Sauer
ATTN: Doc. Con. for Robert Swift
ATTN: Doc. Con. for Tech. Lib.
ATTN: Doc. Con. for E. T. Moore
ATTN: Doc. Con. for Larry A. Behrman

R&D Associates
ATTN: Robert Port
ATTN: Tech. Lib
ATTN: J. G. Lewis
ATTN: Harold L. Brode
ATTN: Cyrus P. Knowles
ATTN: William B. Wright, Jr.
ATTN: Henry Cooper
ATTN: Jerry Carpenter
ATTN: Albert L. Latter

Sciences Applications, Inc.
ATTN: David Bernstein
ATTN: D. E. Maxwell

Science Applications, Inc.
ATTN: Tech. Library

Southwest Research Institute
ATTN: Wildred E. Baker
ATTN: A. B. Wenzel

SRI International
ATTN: Burt R. Gasten
ATTN: George R. Abrahamson

DEPARTMENT OF DEFENSE CONTRACTORS (Continued)

Systems, Science and Software, Inc.

ATTN: Tech. Lib.
ATTN: Donald R. Grine
ATTN: Ted Cherry
ATTN: Thomas D. Riney

Terra Tek, Inc.

ATTN: Tech. Lib.
ATTN: Sidney Green

Tetra Tech., Inc.

ATTN: Tech. Lib.
ATTN: Li-San Hwang

TRW Defense & Space System Group

ATTN: D. H. Baer, R1-2136
2 cy ATTN: Peter K. Dai, R1-2170
ATTN: I. E. Alber, R1-1008
ATTN: Tech. Info. Center, S-1930
ATTN: R. K. Plebuch, R1-2078

TRW Defense & Space Sys. Group

San Bernardino Operations
ATTN: E. Y. Wong, 527/712

DEPARTMENT OF DEFENSE CONTRACTORS (Continued)

Universal Analytics, Inc.

ATTN: E. I. Field

Weidlinger Assoc. Consulting Engineers

ATTN: J. W. Wright
ATTN: Melvin L. Baron

Weidlinger Assoc. Consulting Engineers

ATTN: J. Isenberg

Westinghouse Electric Corp.

Marine Division
ATTN: W. A. Volz